Available online at www.sciencedirect.com

SCIENCE DIRECT

International Journal of Rock Mechanics & Mining Sciences 41 (2004) 785–812

International Journal of Rock Mechanics and Mining Sciences

www.elsevier.com/locate/ijrmms

Damage initiation and propagation in hard rock during tunnelling and the influence of near-face stress rotation

M.S. Diederichs[a,*], P.K. Kaiser[b], E. Eberhardt[c,1]

[a] Department of Geological Sciences and Geological Engineering, Queen's University, 411 Miller Hall, Kingston, Ontario, Canada K7L 3N6
[b] Mining Innovation Research and Rehabilitation Corporation, Laurentian University, Sudbury, Ontario, Canada P3E 6B5
[c] Department of Earth and Ocean Sciences, University of British Columbia, Vancouver, BC, Canada V6 T 1Z4

Accepted 19 February 2004

Abstract

One of the critical design problems involved in deep tunnelling in brittle rock with continuous excavation techniques, such as those utilizing tunnel boring machines or raise-bore equipment, is the creation of surface spall damage and breakouts. The mechanisms involved in this process are described in this paper. The onset and depth of damage associated with this phenomenon can be predicted, as a worst case estimate, using a factored in situ strength value based on the standard uniaxial compressive strength (UCS), of intact test samples. The factor applied to the UCS to obtain the lower bound in situ strength has been shown repeatedly to be in the range of 0.35–0.45 for granitic rocks. This factor varies, however, across different rock classes and must be determined or estimated for each class. Empirical guidance is given for estimating the in situ strength factor based on the UCS for different rock types and for different descriptive parameters. Laboratory testing procedures are outlined for determining both this lower bound strength factor and the upper bound in situ strength. This latter threshold is based on the definition of yield based on crack interaction. These techniques are based, in part, on theoretical principles derived from discrete element micromechanical experimentation and laboratory test results. The mechanisms that lead to in situ strength drop, from the upper bound defined by crack interaction and the lower bound limited by crack initiation, are described. These factors include the influence of tunnel-induced stress rotation on crack propagation, interaction and ultimately coalescence and failure. A case study illustrating the profound impact of near-face stress rotation is presented.

Keywords: Rock damage; Acoustic emissions; Stress change; In situ strength

1. Introduction

In hard rock tunnels at depth one of the primary design issues is the determination of the stress level associated with the onset of wall yield due to boundary compression. For stress levels beyond this point, flaking, spalling and possibly bursting of wall rock can be a costly nuisance and a major safety concern. The development of a tunnel in a stressed rockmass results in a predictable stress concentration tangent to the tunnel wall. In the absence of active support systems, stress conditions at the wall of a tunnel are triaxial with zero wall-normal stress. Typically, for simplified prediction of the onset of wall damage, an equivalent uniaxial stress state is assumed with the maximum compressive stress considered as the dominant index for yield prediction. The starting point in tunnel damage analysis, therefore, is to determine the strength of intact rock using laboratory tests on cylindrical samples as outlined by International Society for Rock Mechanics [1]. This result is then scaled for the rockmass using empirical approaches or by back-analysing carefully documented case histories.

One of the most widely used empirical criteria for scaling the unconfined strength of a rockmass and estimating the confinement–strength relation is the Hoek–Brown criterion [2]. Since its first introduction, the criterion has been modified several times, most recently by Hoek and Brown [3] and by Hoek et al. [4].

*Corresponding author. Tel.: +1-613-533-6504; fax: +1-613-533-6592.
E-mail address: mdiederi@geol.queensu.ca (M.S. Diederichs).
[1] Formerly Swiss Federal Institute of Technology Zürich, ETH, Zürich, Switzerland.

1365-1609/$ - see front matter
doi:10.1016/j.ijrmms.2004.02.003

The generalized non-linear form of the limiting stress criterion for jointed rockmasses is defined by:

$$\sigma_1' = \sigma_3' + \sigma_c \left(m_b \frac{\sigma_3'}{\sigma_c} + s \right)^a, \tag{1}$$

where m_b is the value of the Hoek–Brown "slope" constant for the rockmass, s and a are constants which depend upon the characteristics of the rockmass, and σ_c is the standard uniaxial compressive strength (UCS) of the intact rock pieces. The constants m_b, s and a are determined using the GSI index for the rockmass as in [4]. The UCS of the rockmass is then estimated as:

$$\sigma_{crm} = \left[\exp\left(\frac{\mathrm{GSI} - 100}{9 - 3D} \right) \right]^{(1/2 + 1/6(e^{-\mathrm{GSI}/15} - e^{-20/3}))} \approx \sqrt{\exp\left(\frac{\mathrm{GSI} - 100}{9} \right)}, \tag{2}$$

where the rightmost simplification is for undamaged, massive to moderately joined hard rockmasses. D is a damage factor (0 to 1) for excavation disturbance and GSI (updated recently by Hoek et al. [4]) is a value typically between 10 and 90, increasing with larger block size, fewer discontinuities and rougher/fresher joint conditions [3,5]. Note that the constant, a, reduces to a minimum of 0.5 for high-quality rockmasses with high GSI. GSI can also be related to commonly used rockmass classification systems, e.g., the rockmass quality index Q or the rockmass rating RMR. This yield criteria, along with its plastic flow counterpart [6] can be used to estimate the yield potential and the depth of disturbance for a tunnel.

It is suggested here, however, that this approach is of limited reliability when used for rockmasses with GSI > 75. In these environments, the Hoek–Brown criterion which is formulated with an emphasis on the confinement-dependant strength component of rockmasses, does not adequately account for brittle damage, crack propagation and the inhibition of frictional strength development in near-excavation environments. The origin of the Hoek–Brown criterion is based on the failure of intact laboratory samples and the reduction of the laboratory strength is based on the notion that a jointed rockmass is fundamentally weaker in shear than intact rock. While the concept is sound, the application of the Hoek–Brown criterion to brittle failure has met with limited success [7,8]. Pelli et al. [9] showed that in order to fit the Hoek–Brown criterion to observed failures, the value of m_b had to be reduced to unconventionally low values. Based on microseismic evidence of damage initiation in advance of a circular tunnel, Martin et al. [8] found that m_b should be close to zero with a value of $s = 0.11$ ($1/3\sigma_c$). Similar findings of low confinement dependency were reported by Brace et al. [10], Stacey and Page [11], Wagner [12], Castro et al. [13], Grimstad and Bhasin [14] and Diederichs [15] who all showed, using back-analyses of brittle failure, that stress-induced fracturing around tunnels initiates at approximately 0.3–0.5σ_c and that the critical deviatoric stress for yield is essentially independent of confining stress. This lower bound strength for damage initiation and accumulation is hereafter referred to as σ_{ci}. In addition, these researchers concluded that the lower bound function for rock strength in terms of maximum principal stress is approximated by the simple linear function:

$$\sigma_1 = (0.3\text{-}0.5)\sigma_c + (1\text{-}1.5)\sigma_3. \tag{3}$$

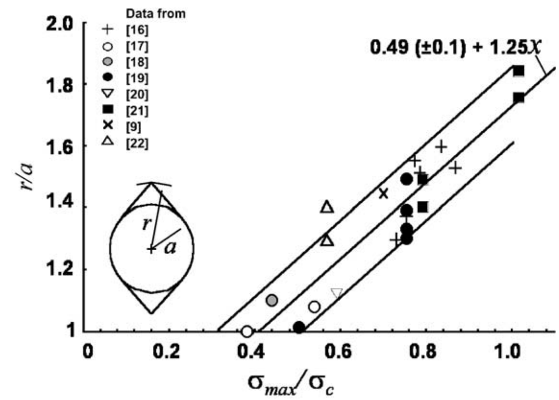

Fig. 1. Case histories for tunnel failure observations based on an equivalent circumscribed circular opening (after Kaiser [16] with data from [9,17–22]). Mean relationship shown with upper and lower bounds representing 95% confidence limits.

A collection of available tunnel overbreak data (compiled by Kaiser et al. [16]) shows that a relationship exists between depth of failure (around a tunnel beyond a circumscribed circular profile) and the maximum induced tangential stress (normalized with respect to the intact rock's standard uniaxial compressive stress). The intercept (indicating no overbreak) of the best fit line occurs at a maximum boundary stress equivalent to 40% of the compressive stress (Fig. 1). Note that this is a lower bound value as unfailed tunnels are not plotted.

This paper will demonstrate how lower bound rock strength for massive brittle rocks is controlled by mineralogy, fabric and grain size. This lower bound concept is not dissimilar to the limit traditionally used for structures in concrete [23]. Whether or not the in situ strength actually degrades to this minimum threshold, however, is a function of heterogeneity, near surface effects, previously induced damage and the effects of tunnel induced stress rotation. These strength reduction mechanisms will also be discussed in this paper.

2. Analogue for rock damage

Since the classic work by Griffith [24], many subsequent researchers, [25,26, etc.] have used a shearing or sliding crack analogue to simulate the initiation of brittle failure although Lajtai et al. [27], based on the observation that, during the middle stages of a compressions test, only lateral dilation of the cylindrical sample is recorded with no axial shortening, suggested that damage initiation was caused by tensile cracking. Rocks are fundamentally weaker in tension than in compression. During compressional loading, tensile cracking will dominate the failure process provided tensile stresses are generated internally and reach the tensile strength. The spalling of massive hard rock, common around underground excavations at depth, and shown in the example in Fig. 2, is the result of this process.

Expanding on concepts introduced by Gramberg [29], Trollope [30] and Cook [31], Diederichs [15] investigated conditions causing tension in a compressive stress field and linked this notion to the relationship between damage initiation and actual rock yield in laboratory and field conditions.

Tapponnier and Brace [32] showed that the length of the cracks, at the damage initiation stage, is limited, by crack–boundary interactions, to the grain size of the rock. Hence, to track the failure process, numerical models should be able to simulate the grain scale. Using the model developed by Cundall et al. [33] and incorporated into the discrete element code PFC [34], Diederichs [15,35] explored the damage initiation process in simulated samples of Lac du Bonnet granite.

In this work, the accumulation of both tensile bond rupture and bond slip were tracked as loads were applied and the results can be used to represent rock by considering particles as mineral grains. PFC treats the rock as a heterogeneous material, bonded together at contacts, with each contact point acting like a pair of elastic springs, allowing normal and shear relative motion. When either a tensile normal-force or a shear-force limit is reached, the bonds break and cannot carry tension thereafter. Broken bonds, which remain in physical contact, can generate frictional shear resistance in response to normal stress. Internal tension at the grain scale is generated by the bond geometry (as per Trollope [30]) and as illustrated in Fig. 3. This geometrical model is an analogue to the actual mechanisms of tensile crack initiation, including situations that mimic the classic shear crack model.

A simulated axial stress versus axial strain curve is shown in Fig. 4. The stress–strain curve shows the characteristic damage initiation (for granite as in [19]) at about 0.3–0.4 of the peak strength and rapid strain softening immediately after peak. Incremental snapshots of crack growth in the top of the figure show that even though the sample is confined with 25 MPa and the final failure mode resembles macroscopic shear zone formation, the total amount of tensile cracking dominates shear cracking by a ratio of approximately 50:1 and that there is little new crack growth after the macroscale failure zone has formed. In other words, the

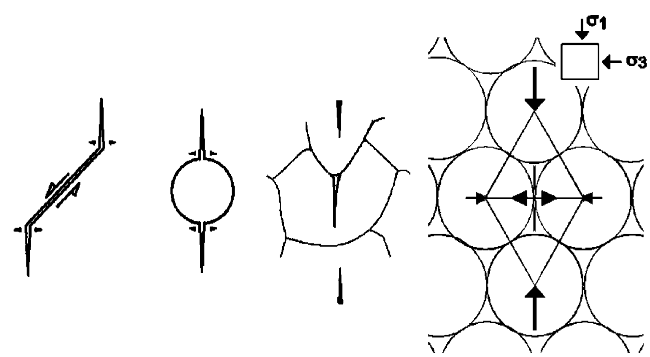

Fig. 3. (Left to right) a sliding-flaw crack initation mechanism, pore or soft inclusion and associated microcracking, grain boundary and indentation crack generation and numerical crack analogue in bonded disc model.

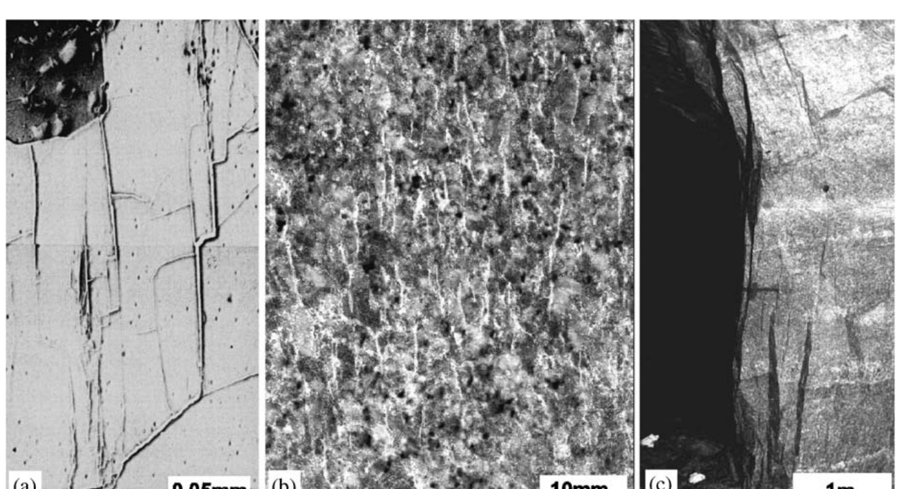

Fig. 2. (a) Axial microcracks in Westerly Granite (after [28]); (b) cracks (dyed white) in compressive test sample of Lac du Bonnet Granite; and (c) excavation spall damage (courtesy AECL-URL). In all cases maximum compression is vertical.

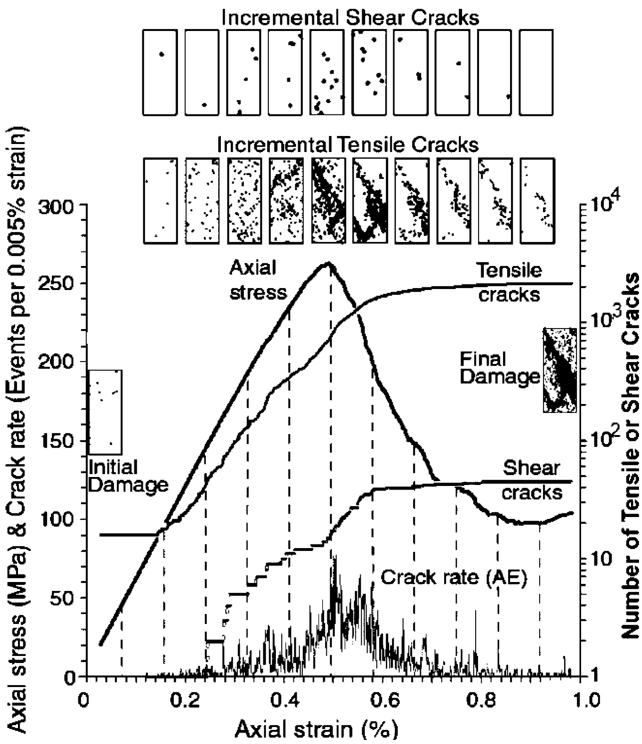

Fig. 4. Discrete element simulation utilizing a bonded-disc analogue for polycrystaline granite. Upper insets show incremental accumulation of shear (top) and tensile cracks during axial compression test with lateral confining stress = 25 MPa (average shear/normal bond strength ratio = 4; average shear/normal stiffness ratio = 0.4, 16,000 initial contacts).

ultimate sample-scale shear zone is really the result of tensile crack initiation, accumulation and interaction.

The numerical simulation in Fig. 4 incorporates heterogeneity in bond stiffness, particle size and bond strength. Heterogeneity (both in grain size and material properties) leads to strain localization as shown by Tang et al. [36] and is also key in generating tensile stresses in a compressive stress field. Furthermore, Diederichs [15] demonstrated that for a system in which unstable propagation of individual cracks is prevented (as is the case with the simple contact-bond model incorporated into these PFC simulations), a consistent statistical relationship exists, for a range of confining stresses, between the stress required for crack initiation and the stress level at which a critical density of accumulated cracks results in crack interaction and yield. The crack interaction threshold is defined as the first point of axial non-linearity or, for uniaxial tests, of volumetric strain reversal. In the PFC model, this point of true yield is coincident with the first occurrence of mutually proximal crack formation as shown in Fig. 5.

In this figure, the number of cracks located within one crack diameter of each other (i.e. crack pairs) are tracked along with other conventional stress–strain indicators. The onset of yield, as coindicated by a change in tangential axial modulus (axial stress–strain non-linearity), by an acceleration of crack accumulation rate and by a peak in the calculated crack anisotropy, is directly related to the first significant occurrence of new cracks forming adjacent to existing cracks. Prior to this point cracks accumulate in a uniformly distributed and independent fashion in accordance with the micro-scale strength and stiffness heterogeneity in the sample. This first interaction event changes the local strain field and creates the potential for damage and strain localization (Fig. 6) and represents the point of first yield.

This finding illustrates that there are two important thresholds to consider in laboratory tests and field observations. The first, crack initiation, is a stress-based limit and forms the lower bound for rock strength. Crack interaction is the onset of true yield and given longer-term loading rates (or standup times) represents the upper bound for in situ rock strength. This threshold (axial stress–strain non-linearity) is coincident with volumetric strain reversal under uniaxial conditions. Volumetric strain reversal under uniaxial loading was shown by Martin [19] to be coincident with the long–term strength (asymptotic stress threshold at failure of samples under ultra-slow loading rates and sustained loading below the sample UCS). The respective stress levels indicative of axial non-linearity and volumetric strain reversal diverge both in the PFC model and in real samples as confining stress increases. An example of this divergence is illustrated in Fig. 7a using data from Lac du Bonnet granite (analysis based on original test data from [19]). A damage initiation threshold from [37] is also plotted on this graph based on lateral strain readings. Other studies, including [38] have shown the damage initiation threshold under uniaxial conditions to be slightly higher than that shown in Fig. 7a.

This crack interaction or initial yield limit is also clearly evident in PFC experiments (Fig. 7b) but is defined in the absence of unstable crack propagation. Geometric ‘‘blunting’’ prevents unstable crack growth in the simple contact-bond particle model and is used here to isolate the impact of crack accumulation without propagation. Note that in Fig. 7b, the interaction limit carries on in a linear fashion into the tensile regime and is clearly inconsistent with actual behaviour. This is due to the requirement, in the model, for crack accumulation in order for yield to occur. Individual interparticle cracks cannot propagate more than an additional grain diameter. Many cracks are thus required for a critical crack density to be reached and for yield to ensue. If cracks, once initiated, are allowed to propagate immediately to failure as observed in actual tensile testing, this would then lead to a curved yield surface in the tensile regime and in the low confinement portion of the compressive regime similar to that observed in Fig. 7a for granite. This is a significant finding from these studies (detailed in [35]), and one that highlights a key

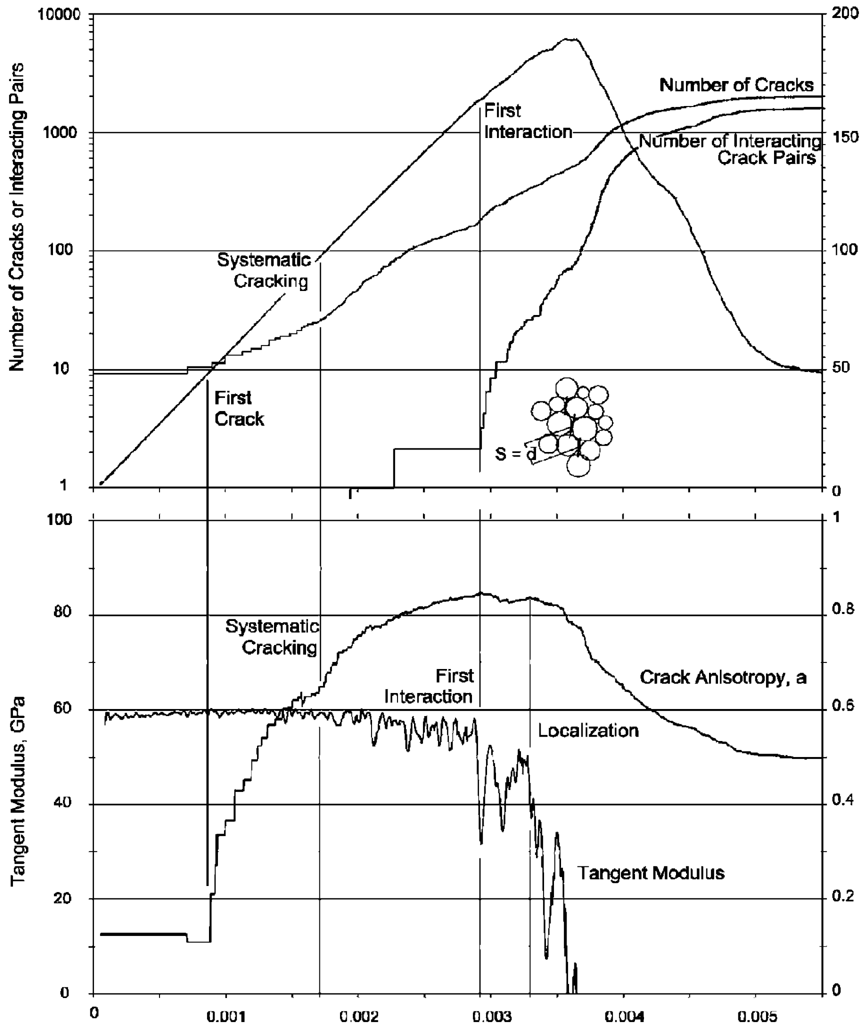

Fig. 5. Discrete element simulation (as in Fig. 4 but with 2.5 MPa of confining stress) showing coincidence of measurable indicators (drop in tangent modulus, maximum crack anisotropy) with increase in proximal crack pairs, signifying the onset of crack interaction (see Fig. 6 for explanation of points A and B).

difference between laboratory testing and in situ yield behaviour (Fig. 8).

As shown in Fig. 1, in situ strength in massive to moderately jointed hard rock approaches a lower bound value of approximately 40% ($\pm 10\%$) of the laboratory strength (or approximately 50% of the yield or interaction threshold). One reason for this response, as illustrated in Fig. 8, is that the geometry of a standard cylindrical test sample provides feedback confinement (through hoop strain) to a dilating crack. A crack initiating in the samples shown in Fig. 8b and c must dilate in order to extend. Dilation creates additional hoop strain within the cylindrical geometry (where the ratio of crack length to radius of surface curvature is large compared to the in situ case in Fig. 8a). This strain, in turn, creates increased confinement normal to the crack and suppresses further dilation.

In the PFC code, the bond-particle lattice and the simple contact-bond model effectively blunts crack propagation. Both situations, therefore, create conditions in which failure occurs primarily by crack accumulation and interaction at essentially limited crack lengths (this was shown by Martin [19]). Fig. 9 contrasts grain-scale damage (initiation) with macroscopic fracture (propagation across numerous grains) in granodiorite. In laboratory samples of low porosity, propagation of cracks across multiple grains often occurs only after crack interaction (yield) has occurred and is often driven by macroscopic shearing and dilation. In situ, however, a number of factors lead to this propagation extending beyond the limits of the grain boundaries and ultimately to larger-scale spalling. The mechanisms and significance of propagation and ultimately, of spalling, will be discussed presently as they pertain to in situ strength reduction.

It is important, however, at this stage to return to the mechanism of damage initiation as it represents an engineering lower bound for in situ strength, as without

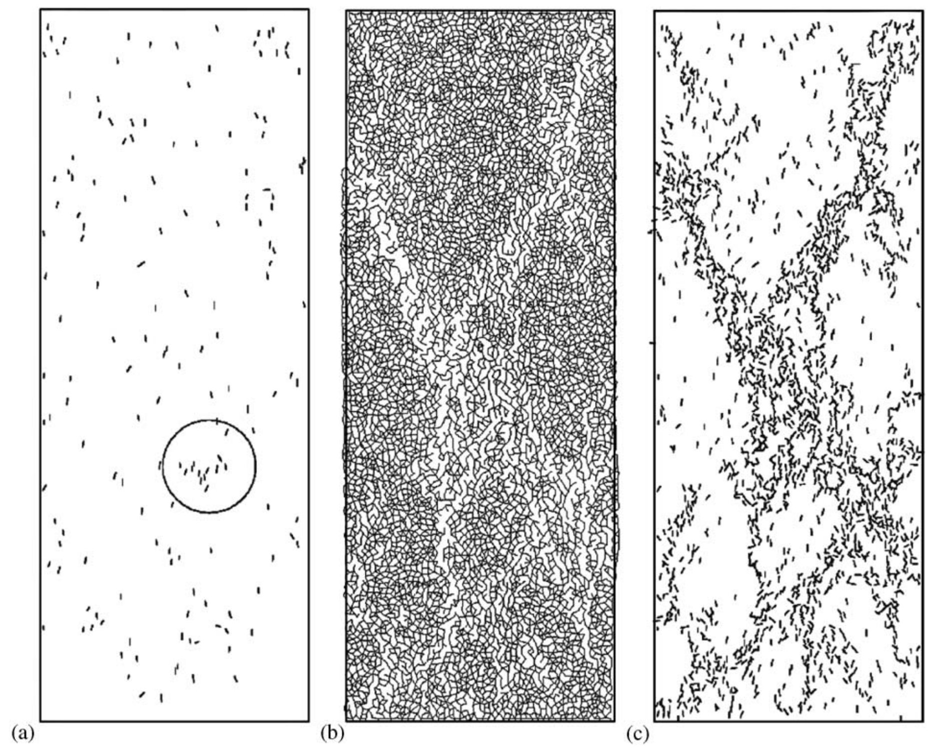

Fig. 6. (a)–(c) Discrete element simulation from Fig. 5, showing (left to right) the first onset of interacting cracks (circled) at point A in Fig. 5, the final bond geometry after failure and representative microcracks (normal to broken contacts) after failure (centre and right image at point B in Fig. 5).

initiation there can be no propagation. Likewise, the crack interaction threshold measured in laboratory tests and therefore under conditions of minimal crack propagation represents a reasonable upper bound for in situ strength. These two thresholds are much more important than the ultimate compressive strength in that they represent true material properties. It is therefore essential to determine, from lab tests, the crack initiation threshold and the crack interaction threshold.

3. Damage thresholds

The PFC simulations of Diederichs [15] demonstrated simple criteria for determining these two thresholds. Eberhardt [39] performed a number of tests on granite, granodiorite and other rock types, incorporating acoustic emission monitoring. The details of the acoustic monitoring procedures are given in Eberhart et al. [38]. For uniaxial loading conditions, the main stages of crack accumulation are shown in Fig. 10.

In Fig. 10, it can be seen that the crack interaction threshold is shown to be coincident with the point of volumetric strain reversal. As discussed, this phenomenological relationship has often been used as an indicator for yield, although the authors suggest here that this relationship is unique to uniaxial conditions, and to non-porous crystalline rocks. Numerical simulations [15] and reanalysis of granite testing by Martin [19] suggest that crack interaction and the onset of localization and yield are not coincident with volumetric strain reversal in confined conditions (Fig. 7).

Eberhardt et al. [38] proposed a methodology for determining damage initiation and interaction thresholds based on acoustic monitoring. The following discussion updates this previous work and reconciles it with the conclusions of Diederichs [15,35] from numerical experimentation. The results of numerical experimentation, using a simple contact-bond model in PFC, provide guidance regarding the identification of the point of systematic crack accumulation and of crack interaction. Eberhardt et al. [38] identified five major thresholds within a typical stress/strain test on rock samples coupled with acoustic emissions monitoring.

Crack closure (σ_{cc}), is the point at which most existing, open and appropriately oriented fractures are effectively closed by the increasing axial stress. This is indicated by the shift in the axial stress–strain curve from incremental rate increase to constant rate increase (linear elastic behaviour). It is also often reflected in a cessation in initial acoustic emissions. There is often an initial flurry of emissions due to seating and sample adjustment, as well as crack closure.

Crack initiation and secondary cracking (σ_{ci1} and σ_{ci2} respectively) mark the onset of new damage. σ_{ci1} is the point where new AE counts first rise above background.

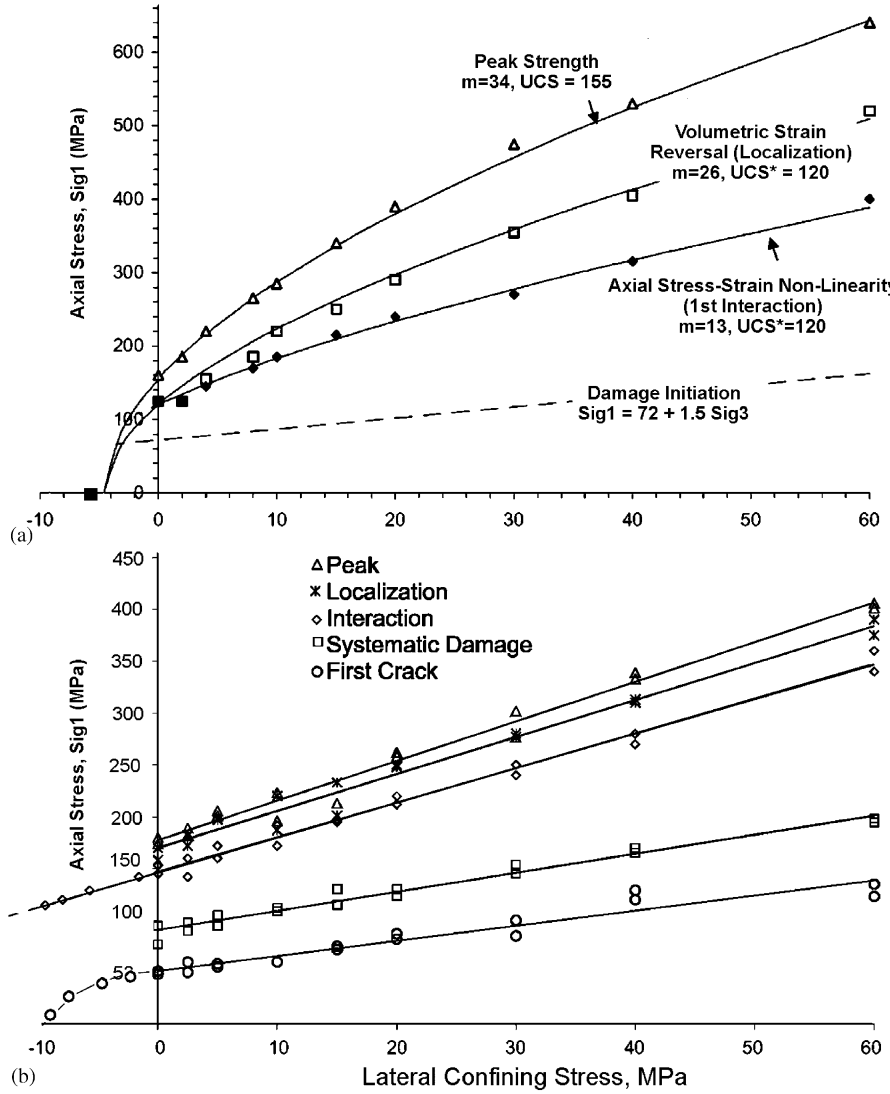

Fig. 7. (a) Initiation, interaction, localization and peak stress thresholds for confined compression tests on granite (granite results); and (b) similar thresholds for discrete element simulations (2D) (PFC simulation results).

It can also be detected through detailed examination of the lateral strain response or the instantaneous ratio of lateral/axial strain rates. Eberhardt identified two initiation thresholds (σ_{ci1} and σ_{ci2}) and proposed that these were related to composite mineralogies. This may be partly the case, although Diederichs [15] demonstrated that the first observable threshold, "First Crack", representing the first onset of distributed cracks not associated with platen interference, is the result of statistical outliers of elemental strength within the sample and is consistent with Eberhardt's σ_{ci1} observations. The second threshold, "Systematic Initiation" , or σ_{ci2} is a true representative limit for the onset of new damage within a sample. The importance of the second threshold, as a material property, is reflected in the results of numerical simulations (PFC) on heterogeneous samples of consistent elemental property distribution (Weibull distribution of strength and stiffness) as shown in Fig. 11. The systematic crack or systematic damage threshold is seen to be less scale dependant and less sensitive to outlier "weak links" within the sample. With respect to increasing stress, the rate of change of the ratio of lateral strain increment to axial strain increment shows a marked increase at this point (Fig. 12). This threshold marks the onset of "continuous detection" of AE and is reflected in a constant rate increase of cumulative acoustic counts with respect to applied axial stress. Hereafter, the systematic crack initiation threshold will be referred to simply as σ_{ci}. This threshold is highly significant as the lower bound for in situ compressive strength near excavations.

Crack Coalescence (σ_{cs}) is the threshold at which axial stress–strain response is observed to become non-linear. Diederichs [15] also showed that this threshold, reflected in the instantaneous tangential stiffness response in Fig. 5, also corresponds to the deviation of log-linear

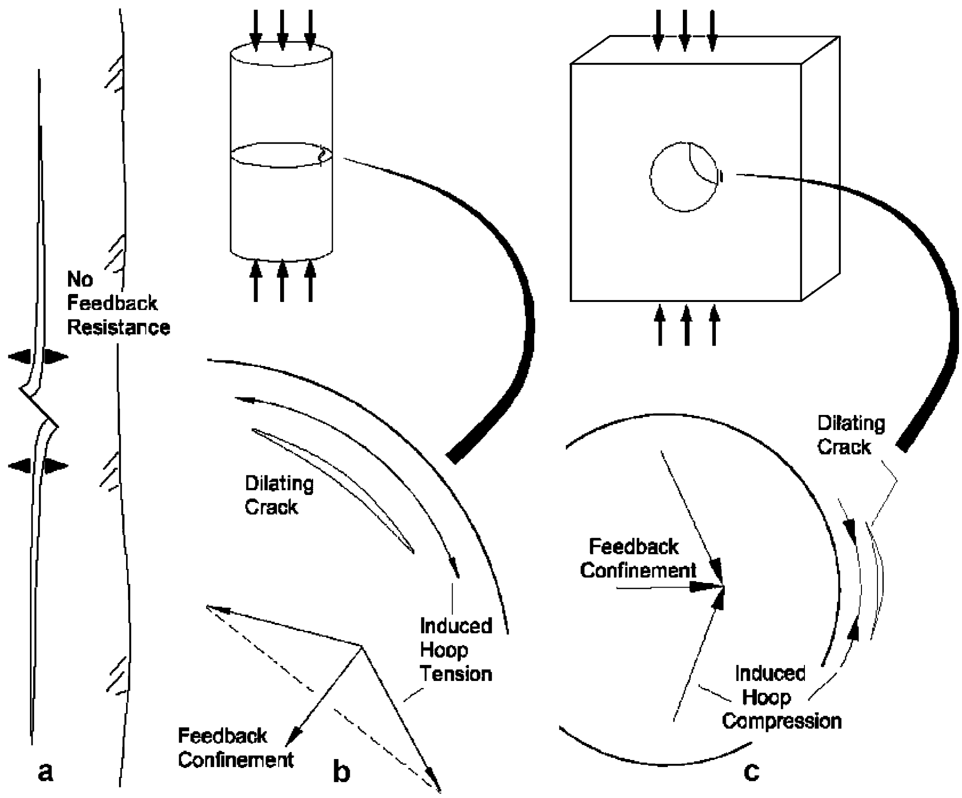

Fig. 8. (a) Unrestricted crack propagation near an excavation boundary (left); (b) crack suppression through feedback confinement in laboratory-scale tests on cylinders (middle); and (c) small boreholes (right).

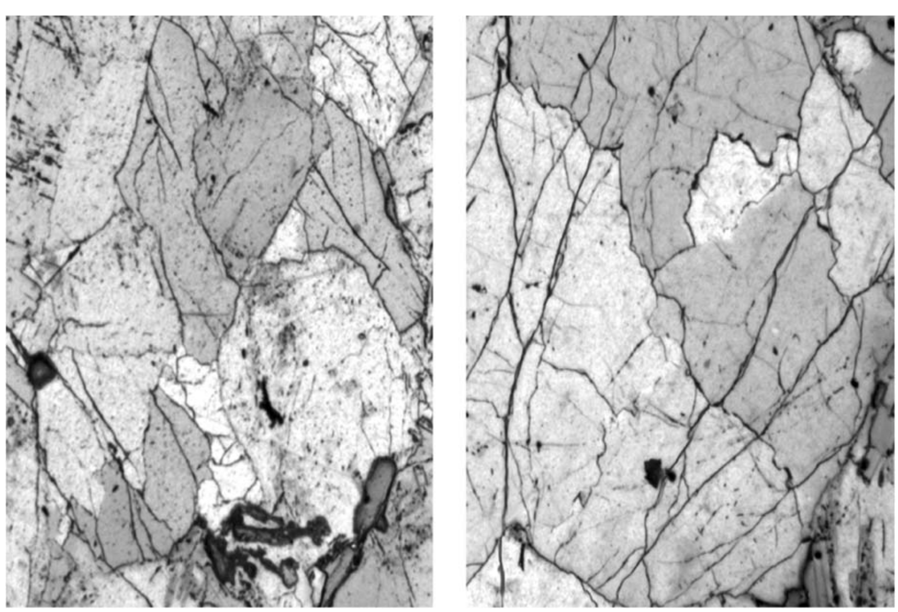

Fig. 9. A granodiorite sample showing (left) grain-scale damage and (right) intergranular crack propagation.

accumulation of acoustic emissions (cracks). As discussed previously, this threshold corresponds to the first significant interaction of accumulating cracks. This "crack interaction" or true yield threshold is clearly indicated along with the other thresholds in the schematic of Fig. 13. It is proposed here that this threshold represents the true upper bound for in situ strength.

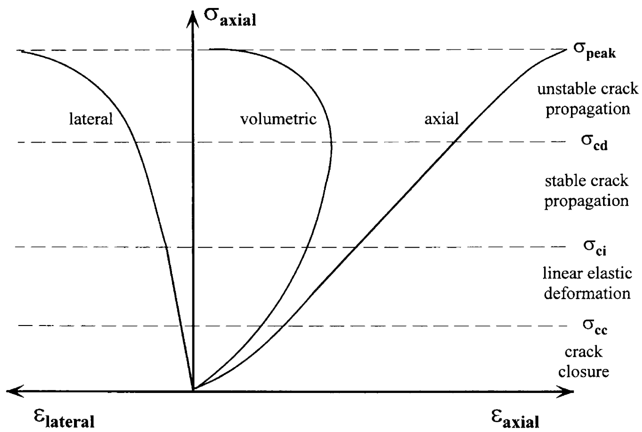

Fig. 10. Stages of stress/strain and acoustic response in uniaxial testing (after Eberhardt et al. [38]).

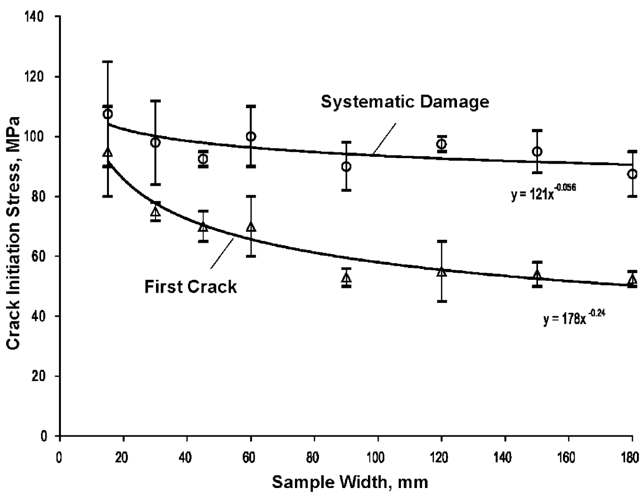

Fig. 11. Relative scale dependency (in numerical simulations) of the stress thresholds for first crack detection and for systematic damage initiation as defined in the text (error bars indicate upper and lower bounds for six simulations at each stage). See text for definition of "first crack" and "systematic damage".

Crack Damage (σ_{cd}) is a final threshold prior to peak strength, identified by a reversal in the volumetric strain response. This "localization" threshold is also evident in PFC testing but is inconsistent and is presumed by these authors to be testing system dependant and not a reliable marker for true yield. One reason for this is that after the initial interaction, the axial strain begins to increase at the same time as the lateral strain rate increase. This combined rate increase leads to a lag in the onset of volumetric strain reversal. This threshold will not be discussed further in this paper.

4. Detection of threshold from real data

The thresholds described in the last section and illustrated schematically in Fig. 13 are not always easy to detect in real data. This is particularly the case where the virgin in situ stresses at the sample location are close to the levels of systematic crack initiation. Observed acoustic emission or AE increases can be due to the Kaiser effect [e.g. 40–42]. These spikes in AE are not generally related to the fundamental material properties of the representative sample but rather to sample unloading history and potentially, to in situ stress magnitudes as randomly distributed and previously unbroken "weak-links" within the crystalline structure are loaded and failed. Often the total event counts related to the Kaiser effect are much less than the increases related to systematic accumulation of new damage during monotonic loading. The Kaiser effect may mask the "first crack" threshold (also the result of random weak links) but should not interfere with the detection of the "systematic initiation" threshold using the technique in Fig. 13, unless the previous in situ stress is close to or exceeds the material's systematic initiation threshold.

Even if the Kaiser effect is not a problem, early non-linear response of partially damaged samples creates some confusion. There will normally be an initial flurry of acoustic activity in the early stages of the test, related to seating, crack closure and other system effects, and this activity may continue up to significant stress levels. Figs. 14 and 15 illustrate a uniaxial compression test response from a granite sample taken from the 240 m level of the Underground Research Laboratory in Manitoba, Canada (the URL facility is described by Martin et al. [43]). There is an initial accumulation of events (over 300 "hits") while a slight increase in event rate (marked A) can be seen at around 50 MPa.This is the "First Crack" threshold illustrated in Fig. 7. A more consistent rate increase (marked B in Figs. 14 and 15) is seen at just under 80 MPa and marks the onset of systematic damage initiation. A constant increase in acoustic event rate is reflected in the constant slope above 80 MPa in Fig. 14. Deviation from this constant log-slope (i.e. a sharp increase in the second derivative of cumulative event count versus applied axial stress) indicates the onset of crack interaction (σ_{cs}), indicated as threshold *C* in Figs. 14 and 15.

A different response is shown in Fig. 16. Here, a granodiorite sample from the same level (depth) is tested in uniaxial compression. The initial increase in acoustic emissions (related to crack closure and other system effects) gradually drops off. A bilinear construction reveals the point of systematic crack initiation at just over 110 MPa. This is followed, as before, with a log-linear accumulation response (constant rate increase with respect to applied stress increment). Deviation from this constant rate increase signifies the onset of crack or damage interaction. Fig. 17 shows the relationship to other measurable parameters. The development

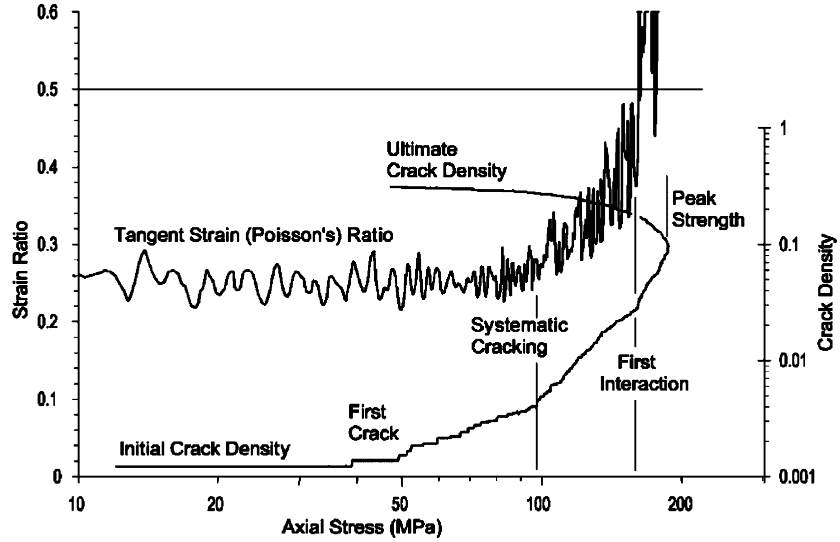

Fig. 12. Change in tangent strain ratio (ratio of lateral and axial strain rates) and crack density χ ($\chi = A^{-1}\Sigma d^2$ where d is the crack length and A is the 2D sample area) with respect to applied axial stress for discrete element simulations.

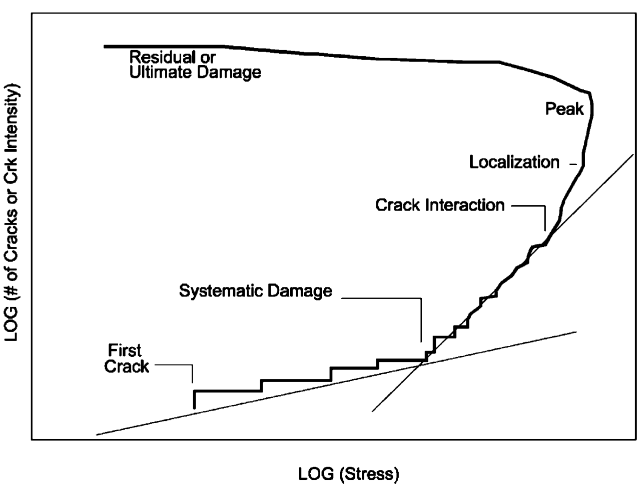

Fig. 13. Schematic illustration of damage threshold determination from standard compression tests and acoustic emissions.

of tangent Poisson's Ratio (instantaneous relationship between lateral strain increment and axial strain increment) is complex. There is no initial plateau as illustrated in the simulated data of Fig. 12. Close inspection, however, reveals that the onset of systematic initiation corresponds to the point at which the second derivative (of the Poisson's ratio versus axial stress plot) changes from negative to positive. This is the point of inflection in Fig. 17. It is not as easy in this case, to identify the onset of crack interaction from the tangential axial modulus (axial stress increment over axial strain increment) although a minor drop in modulus is normally evident. The AE data is more conclusive in this case.

5. Lower bound in situ strength

There are a number of factors at work in situ that combine to reduce the upper bound strength, indicated by the damage interaction threshold, to the lower bound represented by systematic damage initiation. Some of these will be discussed in subsequent sections. It is most important from an engineering point of view to determine the lower bound value for in situ strength. This material property is reflected in the acoustic emission response as discussed in the previous sections. It is still convenient to express this threshold as a ratio of the UCS for standard cylindrical tests on undamaged specimens [1]. For granitoid rocks the ratio of lower bound strength or systematic damage initiation is approximately 0.35–0.5.

This lower bound ratio is not, however, universal across all rock types. It is dependent on a number of factors including scale effects, confinement differences between the field and the lab, surface interactions, material inhomogeneity, strain rate, creep and stress rotation during excavation. Crack initiation and crack propagation are normally controlled by separate mechanisms within rock materials. All of these influences are in part controlled by the relative potential for crack initiation and for crack propagation. Materials which readily permit crack propagation in unconstrained conditions will have a lower in situ or *field strength ratio* ($\mathrm{FSR} = \mathrm{UCS}_{\mathrm{in\,situ}}/\mathrm{UCS}_{\mathrm{lab}}$) than those that naturally suppress propagation. Based on petrological, mechanical and observational evidence, the critical determining factors for FSR include:

Rock type: The type of rock (e.g. igneous, meta-clastic, sedimentary, chemical precipitate and meta-carbonate)

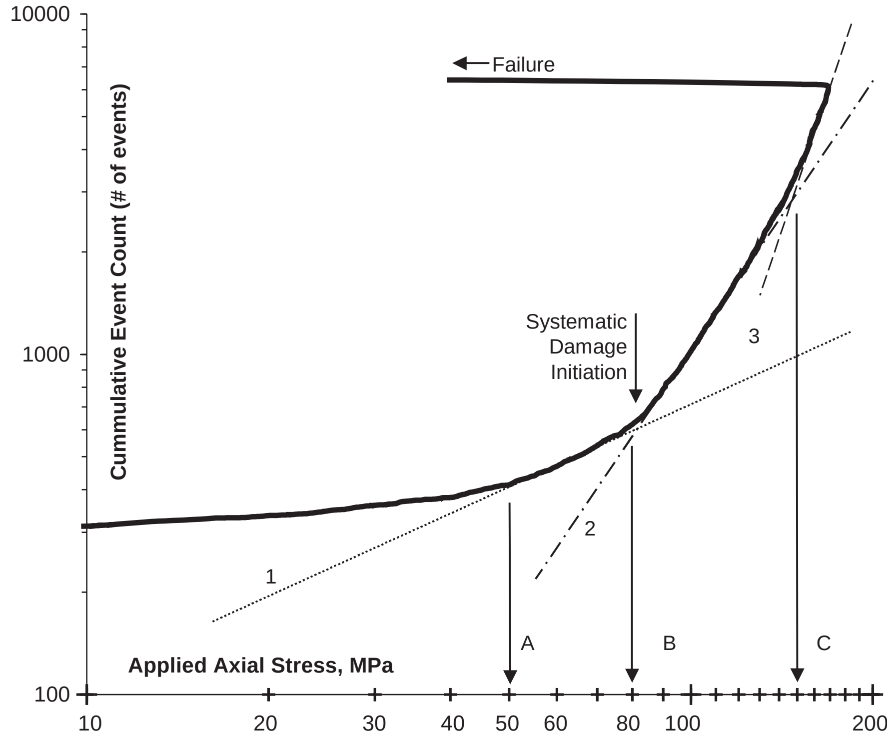

Fig. 14. Applied axial stress and cumulative acoustic event count (log–log plot) for Lac du Bonnet granite (240 m depth) showing linear trend intersections corresponding to damage thresholds: A = first crack; B = systematic damage initiation and C = crack interaction.

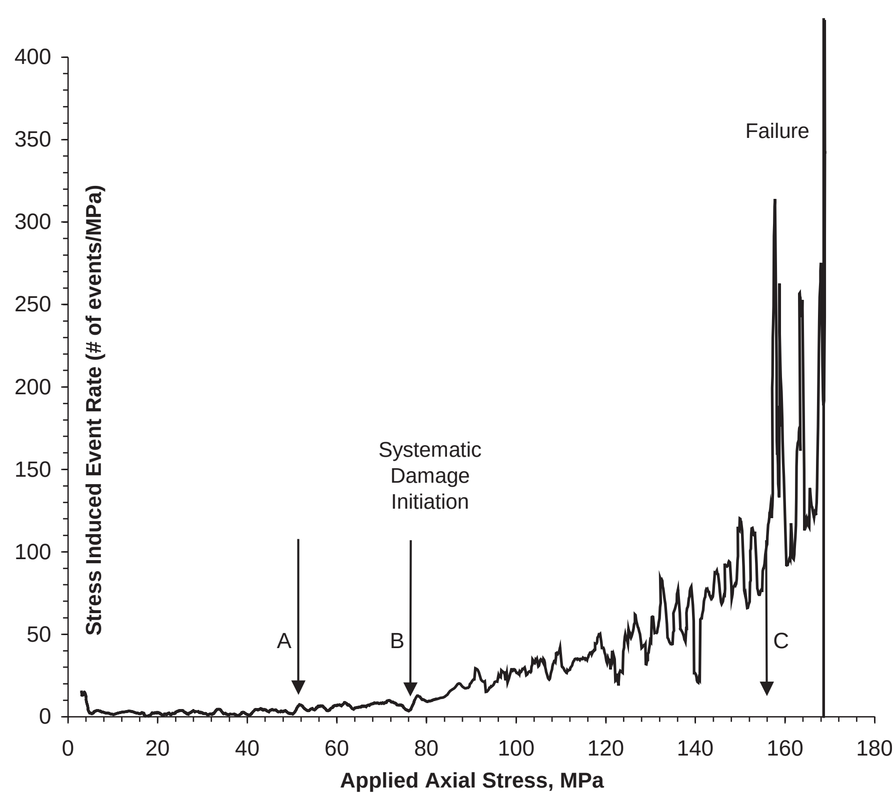

Fig. 15. Same test as in Fig. 14 showing event rate per stress increment.

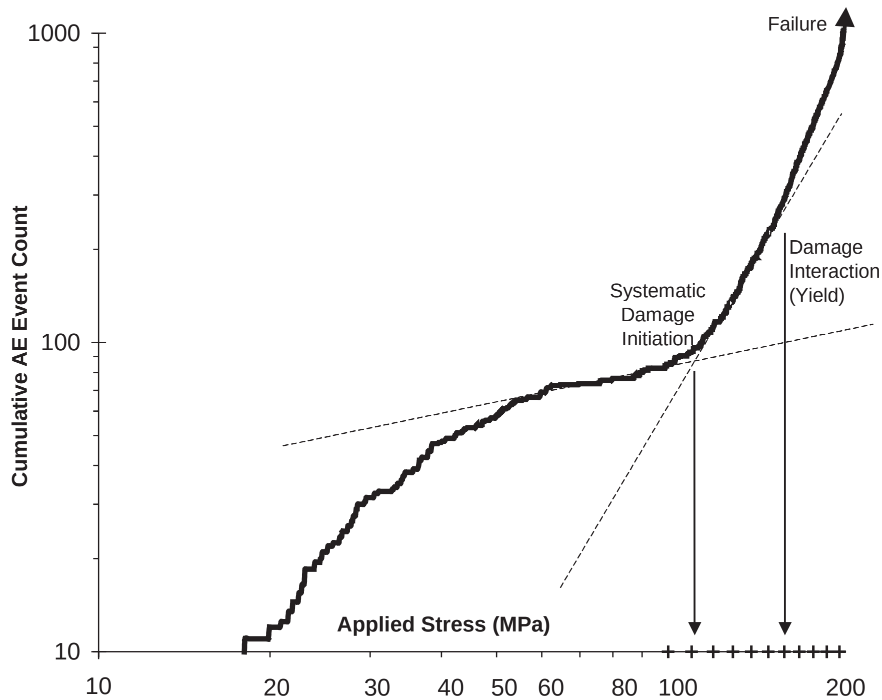

Fig. 16. Applied stress versus cumulative event count for fine grained granodiorite samples (240 m level at URL, Pinawa).

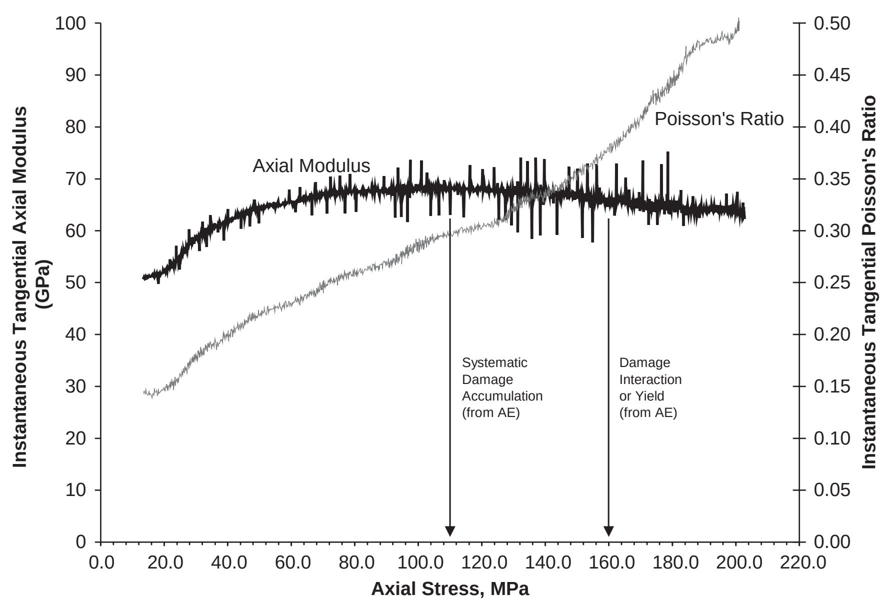

Fig. 17. Axial modulus and tangent Poisson's ratio as functions of applied axial stress (same sample as Fig. 16).

influences the degree of heterogeneity and the grain boundary characteristics. Heterogeneity generates grain interactions which promote early initiation and which also lead to confinement heterogeneity and propagation potential within the sample. In igneous or meta-clastic rocks, the welded grains allow for cross-boundary propagation. In metamorphic rocks fabric generation typically strengthens the role of intra- and inter-granular slip and reduces the role of crack propagation. In clastics, intra-granular and cross-contact crack propagation is not likely. Sulphide ores are a special case. For higher grades of metallic mineralization, dislocation slip dominates rather than brittle fracture. For this reason a special set of factors was proposed and verified by Suorineni and Kaiser [44].

Grain size: In general, larger grain or clast sizes increase heterogeneity and reduce the initiation threshold. For large grains however, such as in a pegmatite, mechanical instability reduces the laboratory peak strength for typical sample scales. This results in an apparent increase in the initiation/peak stress ratio.

Foliation and fractures: For foliation oblique or parallel to the direction of major compression, the laboratory yield value represents the in situ strength as slip on the foliation dominates. For loading normal to foliation, the strength reduction factor calculated as for other rocks applies. It is best to consider the range between these two strength estimates. Late stage brittle fractures of sample and excavation scale are left out here as the bulk of this discussion relates to unfractured rock. Ongoing research by the authors is aimed at resolving the impact of fabric beyond the grain scale.

Mineralogy: Available evidence suggests that minerals with good cleavage reduce in situ strength. In addition, a mixture of high cleavage minerals and quartz results in a mechanical incompatibility which also degrades strength. Mafic minerals, should theoretically give more consistent mechanical behaviour and a higher in situ strength ratio, although testing is limited in this area.

Minor minerals and phyllosilicates: Micas, chlorites and other minor minerals, in small amounts, create damage nucleation sites and reduce in situ strength. Higher concentrations tend to suppress unstable crack propagation and increase the in situ strength ratio.

These factors can be summarized in a classification scheme outlined in Table 1. Factors F1–F4 are assigned according to the characteristics of the rock in question and multiplied to obtain FSR. A number of caveats and limitations are given at the end of Table 1. Most significant is the effect of stress rotation around a tunnel face and its effect on the depth of failure and apparent in situ strength. This will be discussed presently.

More testing is needed with more attention paid specifically to damage initiation. Nevertheless, available data in the literature and new data from Eberhardt [39] and others can be used to verify this preliminary strength classification scheme. Recalling that the standard laboratory UCS is still used here as a datum, the real lower bound in situ strength is assumed to directly correlate with the systematic damage initiation threshold observed via acoustic emission or strain monitoring data in these tests. A summary of verification data is given in Table 2. Factors F1–F4 were assigned based on the petrological descriptions in the associated literature, FSR was calculated from these factors and compared with the actual damage initiation threshold recorded in these tests. The data is further summarized in Fig. 18 and while more testing is needed, it shows an encouraging correlation.

6. In situ strength reduction mechanisms

The foregoing discussion related to a lower bound in situ strength value. The engineer can be secure in the knowledge that until the rock has been stressed beyond the damage initiation threshold, fractures cannot propagate and stress-induced failure cannot occur through intact rock. It is not as confidently stated, however, that the in situ strength will always reduce to this lower bound value. Fig. 1 showed examples of depth of failure measurements. What was missing in this Fig. was the data set of unfailed tunnels. These cases are seldom recorded in rock mechanics literature. The test tunnel data from the Underground Research Laboratory (data points referenced as [18] in Fig. 1) represents failure in the granites along the tunnel. Granodiorites, more homogenous and finer grained, were equally prevalent along this tunnel and showed no failure in spite of an FSR (σ_{ci} /σ_c) of 0.47 (see Table 2) and a calculated boundary stress ratio, σ_{max}/σ_c of 0.7. It is apparent then that while the minimum or lower bound in situ strength is given by σ_{ci}, the actual strength can be larger up to a maximum given by the crack interaction threshold.

Diederichs [15] described and quantified a number of mechanisms that, in combination, reduce the crack interaction threshold near excavations in situ including:

- Scale effects
- Effectively reduced local confinement due to open cracks
- Crack – surface interaction (and enhanced crack propagation)
- Unloading or pre-existing damage
- Damage due to stress rotation
- Heterogeneity and induced local tension

Scale effects (not including macroscale discontinuities) can be accounted for statistically and are not on their own sufficient to reduce strength by the required magnitudes. Of course larger initial flaws that may be present in an excavation scale rockmass will drive larger induced tension cracks and thereby weaken the material. Scale-dependent energy release is a factor once localization has occurred but does not significantly affect the behaviour prior to crack interaction. Cracks (and joints) that are allowed to relax and dilate adjacent to an excavation effectively reduce the local confining stress to zero farther into the rock beyond the boundary, reducing apparently confined strength to the uniaxial minimum. This local confinement reduction leads to enhanced crack propagation as well. In addition, fracture mechanics can be employed ([35,50]) to demonstrate that the presence of a nearby free surface creates enhanced crack propagation due to "beam" effects, over and above the influence of confinement reduction alone, leading to enhanced crack propagation.

Table 1
Estimation of the in situ strength using unconfined compression test (UCS)

General Type*		Igneous or metavolcanic**	Meta–clastic**	Clastic** including mudstone	Chemical precipitate*
	*$F1$	0.8	0.85	0.9	0.7
Grain size		Microscopic	Medium visible to 2 mm	Coarse 2–8 mm	Pegmatite >8 mm
	**$F2$	0.85	0.8	0.75	0.85
Dominant mineralogy		Dominant K-spar or calcite	$\{$K-spar + calcite$\} > 0.8 \times \{$quartz + plag$\}$	Predominantly quartz + plagioclase	Dominant mafics
	$F3$	0.75	0.8	0.85	0.85
Micas, chlorites, clay minerals, graphite, sericite, minor sulphides and voids		$<2\%$	2–10%	10–20%	$>20\%$
	***$F4$	0.9	0.75	0.85	0.9

Total ratio $\mathrm{FSR} = F1 \times F2 \times F3 \times F4$.
(UCS in situ) = FSR $\times$ (UCS lab).
FSR represents horizontal intercept of damage limit in Fig. 1.
Note: *DAMAGE*: It is necessary to obtain undamaged samples. $E_{\mathrm{secant}} > 90\%$ of $\mathrm{E}_{\mathrm{Tangent}}$ at 75% UCS.
STRESS PATH:
If UCS(in situ) thus calculated (FSR x $\mathrm{UCS}_{\mathrm{lab}}$) is greater than $2/3 \times \sigma_{\max}$ (tangential stress around opening) then use default combined FSR = 0.7 or $\sigma_{\mathrm{cd}}/\mathrm{UCS}$.
See subsequent section on stress rotation for explanation of this adjustment.

*This procedure is not applicable to evaporites (salt, potash, etc), highly foliated, fractured or shistose rock.

**If texture is glassy use combined FSR = 0.8.

***For massive sulphides (based on [43]); High Grade Combined FSR = 0.7; Med. Grade Combined FSR = 0.6; Low Grade (use above table with sulphides for $F3$).

Table 2
Verification of rating system by comparison with measured thresholds

	Measured	Predicted				
	σ_{init}/UCS	FSR	$F1$	$F2$	$F3$	$F4$
Indiana Limestone [19]	0.320	0.315	0.70	0.80	0.75	0.75
Concrete [23]	0.330	0.335	0.70	0.85	0.75	0.75
Lilydale Limestone [45]	0.345	0.357	0.70	0.80	0.85	0.75
Pink Granite [39]	0.360	0.360	0.80	0.75	0.80	0.75
Grey Granite [39]	0.360	0.360	0.80	0.75	0.80	0.75
Marble [46]	0.380	0.378	0.70	0.80	0.75	0.90
Norite [47]	0.405	0.408	0.80	0.80	0.85	0.75
Fountainbleau Sst [48]	0.454	0.459	0.90	0.80	0.85	0.75
Granodiorite [39]	0.469	0.462	0.80	0.80	0.85	0.85
Pegmatite [39]	0.475	0.462	0.80	0.85	0.80	0.85
Westerly Granite [10]	0.476	0.462	0.80	0.80	0.85	0.85
Chloritized Norite [47]	0.496	0.490	0.80	0.80	0.85	0.90
S.A. Quartzite [49]	0.500	0.491	0.85	0.80	0.85	0.85
Medium Sandstone [40]	0.500	0.488	0.90	0.85	0.85	0.75
Berea Sandstone [39]	0.564	0.553	0.90	0.85	0.85	0.85

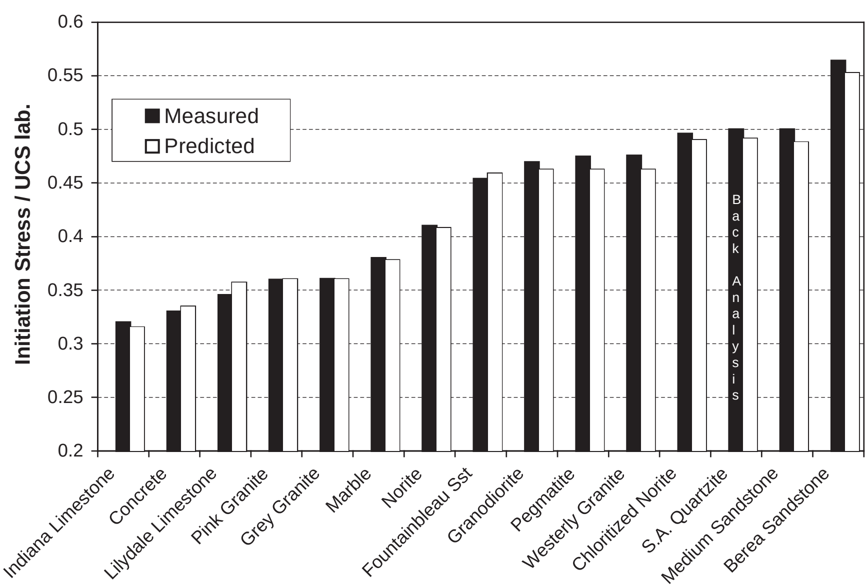

Fig. 18. Correlation between estimated minimum in situ strengths and measured crack initiation thresholds from Table 2.

Heterogeneity, damage, stress rotation will be discussed in the following sections.

The stress threshold for crack initiation is unaffected by these factors (with the exception of scale effects for small samples). The cumulative impact of these mechanisms, however, is to reduce the in situ yield strength, near excavation boundaries, to a lower bound defined by the threshold for crack initiation. The important common element in all of these mechanisms is the impact on the potential for newly initiated extension cracks to propagate longer distances in a confined medium, ultimately breaching the grain boundaries and becoming meso-cracks, the harbingers of spalling failure. Using a statistical model, based on a serial–parallel combination of weak-links as introduced by Jardine [51] and adapted by Diederichs [15], the effect of crack propagation can be schematically estimated (here for a 2D sample):

$$\sigma = \sigma_0(-\ln(1-(1-(1-P_V(\sigma))^{(V_0/2V(L^*)^2)})^{1/2}))^{1/m} + \sigma_i, \quad (4)$$

where σ is the stress level at which crack interaction occurs with the specified probability P_v σ_0, σ_i, m are statistical parameters for elemental strength (Weibull distribution), V_0/V is the ratio of sample size to elemental dimension (grain size), and L^* is the relative crack extension length (with respect to grain size or

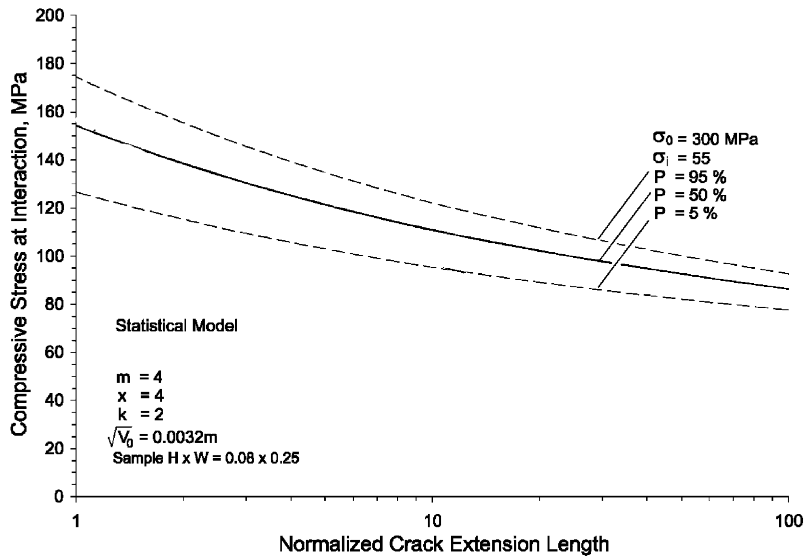

Fig. 19. Statistical impact of increasing propagation length on the interaction threshold for accumulating cracks. Crack extension length (normalized to initial grain size) represents the instantaneous propagation of each additional initiating crack.

initial flaw length). The effect of crack length on crack interaction probability and therefore on yield stress is schematically demonstrated in Fig. 19 using parameters calibrated for URL granite. It is clear then that any mechanism that increases the potential for crack propagation is a major factor in the reduction of in situ strength (recall from Fig. 8 that such propagation is hindered in a standard laboratory test configuration).

7. Heterogeneity and crack propagation

Cho et al. [52] present a summary of fracture mechanics models (open and sliding crack flaw models) that clearly demonstrates that while extension crack initiation can occur, readily within a confined medium, the extending cracks are easily halted as they extend into the confining stresses away from the initial flaw. For true crack propagation to occur the confining stress (normal to the extending cracks) must be near to or less than zero. Fig. 20 illustrates that this is a significant reason why cracks may extend readily through a crystal grain, once initiated, but cannot continue across the grain boundary without significant increases in driving stress or reduction in confinement beyond the grain scale.

In this simulation, generated in PFC using discs of identical diameter and a process of "frictionless consolidation", pseudo-crystals form naturally in the simulated solid. Points A, B, and C illustrate the resultant twinning planes, grain boundaries and uniform crystal lattices that result. If stress is applied to the resultant polycrystalline solid it can be seen that consistency of force transfer exists within grains that show local tensile forces between model particles. If a crack is induced within these grains it will easily propagate throughout the crystal before being confined and halted at the grain boundary by a different internal stress regime within the neighbouring grain.

In a larger-scale simulation, in which the model particles represent the individual grains in a random assembly, the particle diameters and bond stiffnesses are varied to create a heterogeneous assembly. Measurement circles are overlaid onto the sample to calculate local stress tensor samples from the contact forces within the sample assembly as per [34]. The assembly and the grid of measurement circles is shown in Fig. 21. This sample is confined by 3 MPa of confining stress and 140 MPa of applied axial stress. The regions inside the darker contours (contours represent 5 MPa increments of minor principal stress) are in tension. These would represent zones of enhanced crack propagation in a real sample.

Even at higher confinements levels, zones of tension persist. Fig. 22 represents a large PFC sample ($\sim$8000 discs) confined by a nominal lateral stress of 20 MPa.The points in the Fig. represent sampled stress states at two different intervals of applied axial stress. The elliptical limits represent three standard deviations of distribution about the nominal or applied stress state. It can be seen that there are still significant numbers of zones that are effectively in tension (represented by data points to the left of the y-axis).

A number of such simulations were performed at different confining stresses. Results at a number of axial stress levels are plotted in Fig. 23 along with the known model thresholds for initiation, interaction and failure. While it is difficult to know exactly how much tensile

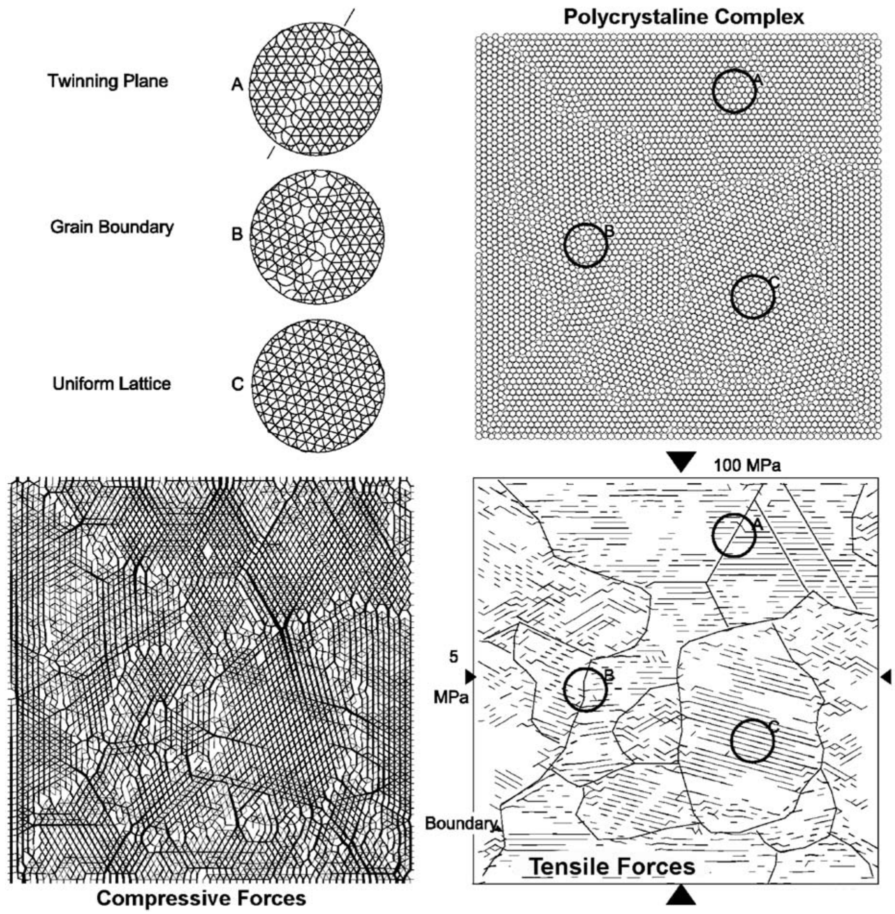

Fig. 20. Simulation of deviatoric stress application to a crystalline solid.

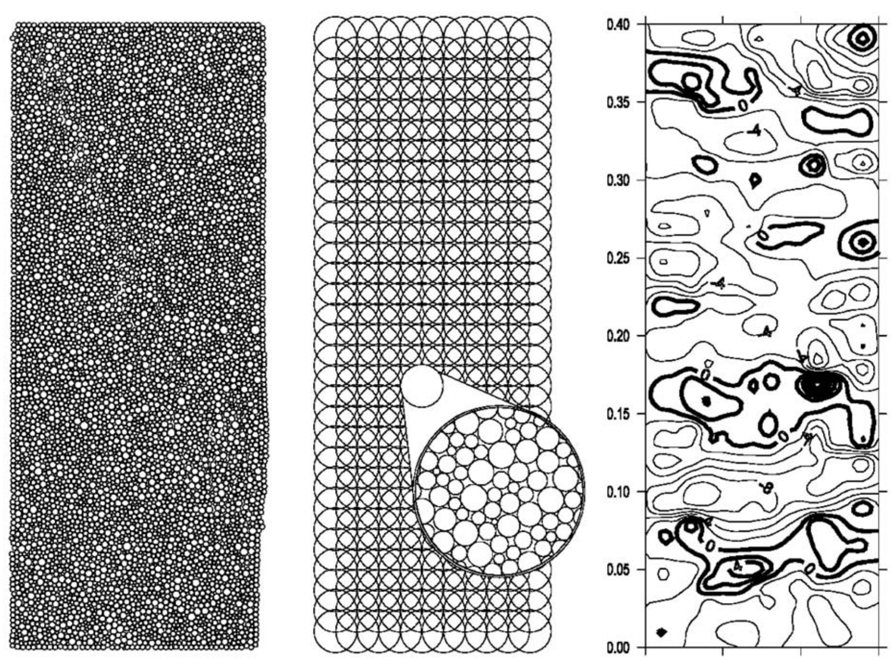

Fig. 21. PFC simulation (left) with same parameters as in Fig. 4. Stress tensor averaging circles (middle) and calculated local minor principal stress contours (right) at 140 MPa of applied axial stress and 3 MPa of confining stress. Areas in side thick contour lines are in tension.

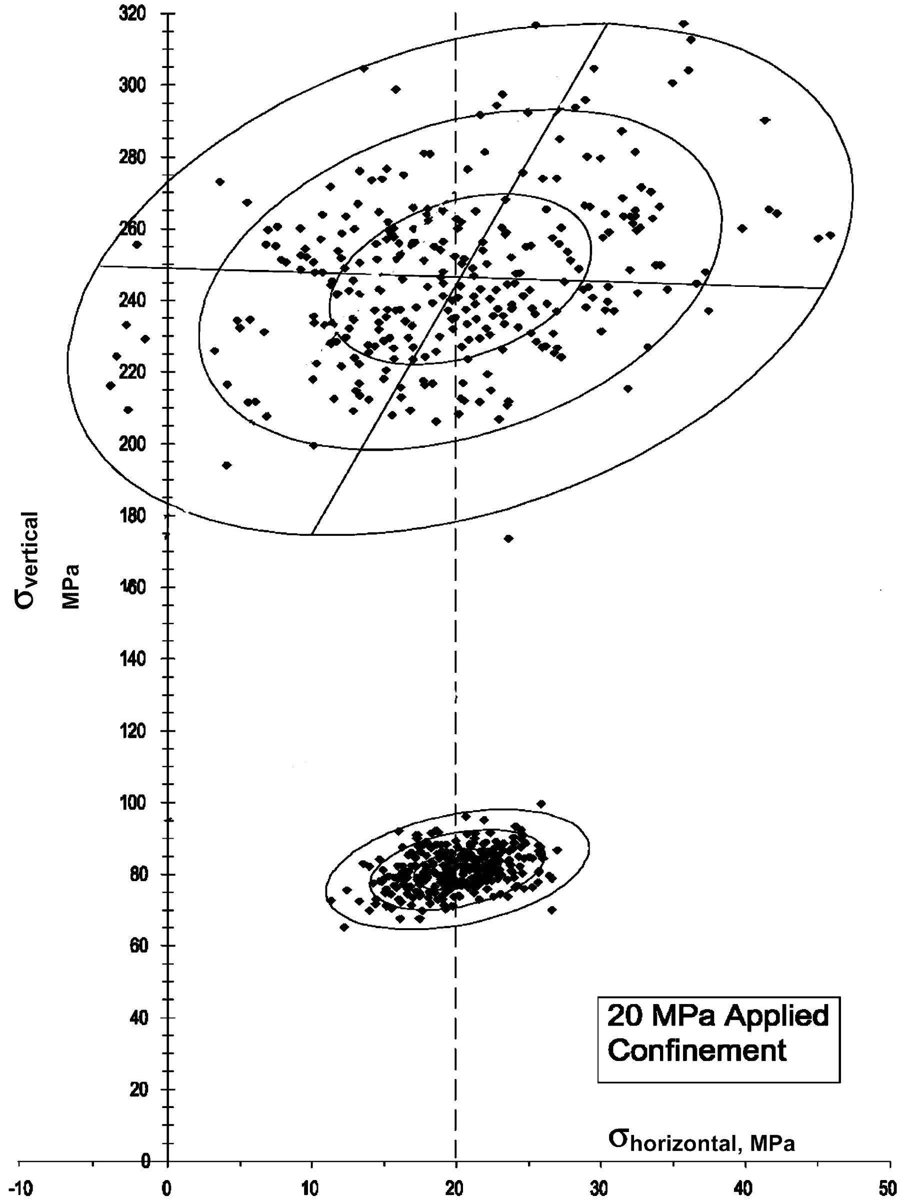

Fig. 22. PFC simulation of confined compression test. Data represents sampled local stresses as per Fig. 21. Lower cluster represents an applied axial stress of 80 MPa. Upper cluster represents an applied stress of approximately 250 MPa. Applied lateral confining stress is 20 MPa. Dashed line represents nominal or mean stress path. Concentric ellipses represent first, second and third standard deviation of calculated local stresses about the mean. In the upper cluster, point to the rights of the vertical axis represents local tension within the sample.

coverage is significant, limits are plotted for 0.1%, 1% and 10% spatial coverage. That is, for the 10% line, any nominal confined stress state on this line will result in a heterogeneous sample with 10% of its area (2D) under actual tensile stress, and so on. The stress ratio ranges indicated for these three coverage limits are reasonable and correspond to those first proposed by Hoek [53].

This stress ratio limit will hereafter be called the spalling limit. In other words a stress state ($\sigma 1, \sigma 3$) above the crack initiation threshold and to the right of this spalling limit has the potential for premature yield due to strength reduction caused by unstable crack propagation. In practice, the slope of the critical spalling limit (which can only be determined empirically at this point) will vary according to the degree of micro-, meso- and macroscale heterogeneity within the rock and rockmass and a number of external factors including damage and stress rotation. Greater heterogeneity, more prior damage and unfavourable stress rotation effects will lead to a shallower spalling limit in Figs. 23 and 24 as effective tensile regions dominate behaviour at higher nominal levels of confinement. If this is the dominant mechanism of strength reduction, a piecewise compound yield surface will be observed in the field as graphically illustrated in Fig. 24.

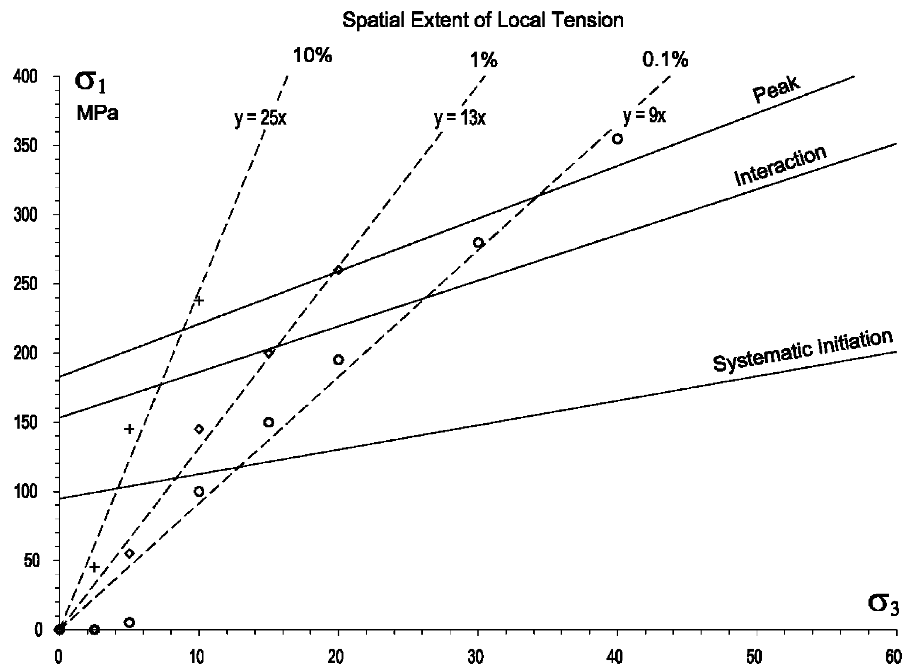

Fig. 23. Strength thresholds (——) and confinement ratio contours (– – –) corresponding to areal percentages (2D simulated sample) of actual local tensile stress occurrence within nominally confined samples at elevated deviatoric stress.

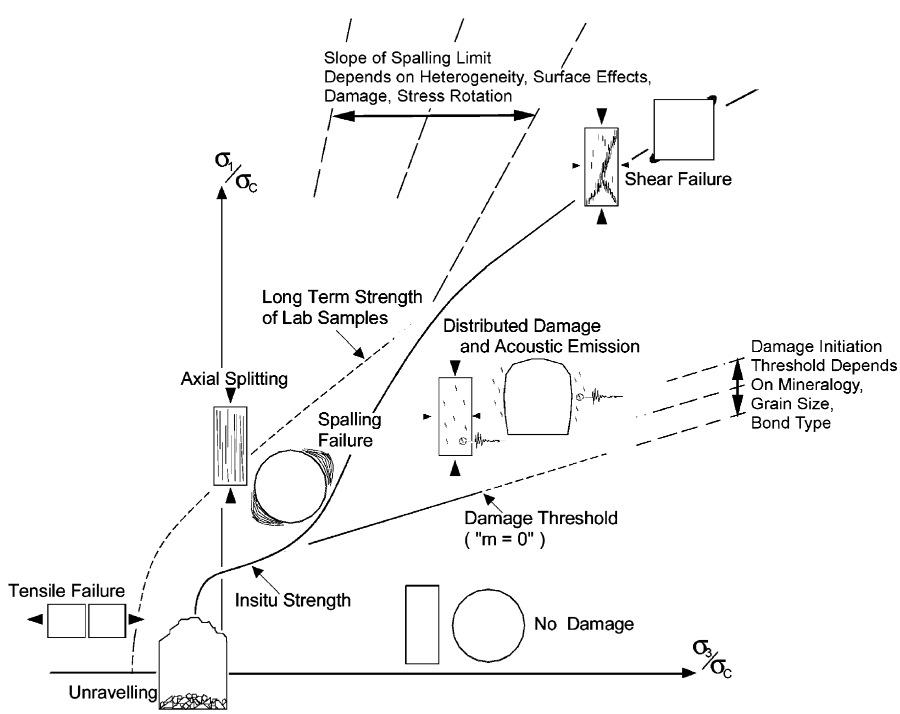

Fig. 24. Composite in situ strength envelope for hard rock (solid curve), composed of segments corresponding to upper bound strength (high confinements), lower bound strength or damage initiation (low confinements) and a transition zone related to the spalling limit (after Diederichs [35]).

8. Effect of existing or previously induced damage

Pre-existing grain-scale damage to rock can occur in situ during tectonic processes, during uplift and stress change and during the excavation process (the stress path around an approaching tunnel face is very complex and will be discussed presently). Rock which has been previously subjected to damage or rock at a later stage in its excavation-induced stress history will be substantially weakened. This was observed in tested samples containing profound unloading damage [54]. Crack initiation readings are difficult to obtain in previously damaged samples due to the persistent behavioural non-linearities associated with crack closure. PFC simulations, on the other hand, allow for direct measurement of new damage initiation. Results on large test samples with varying degrees of initial crack damage show that while crack initiation strength is reduced by the presence of initial damage, the threshold for systematic crack damage initiation is less sensitive (Fig. 25). Only a small percentage of the pre-existing damage may be favourably oriented to act as initiating flaws for new cracks. The presence of these cracks, however, reduces the need for new crack accumulation in order to achieve the critical crack intensity for interaction. In these models, crack intensity is calculated simply as $\chi = A^{-1}\Sigma d^2$ where d is the crack length and A is the 2D sample area.

The effect of pre-existing crack orientation can be investigated using the PFC model (recalling that crack propagation is significantly inhibited in this model). A number of simulations containing pre-existing cracks (broken bonds) with a range of preferred orientations, were tested in uniaxial compression. Results are shown in Fig. 26. Here the orientation of the principal anisotropy represents the preferred orientation of the crack normal with respect to the horizontal. Major principal stress direction during renewed loading is vertical. It can be seen that the effect of oriented cracks

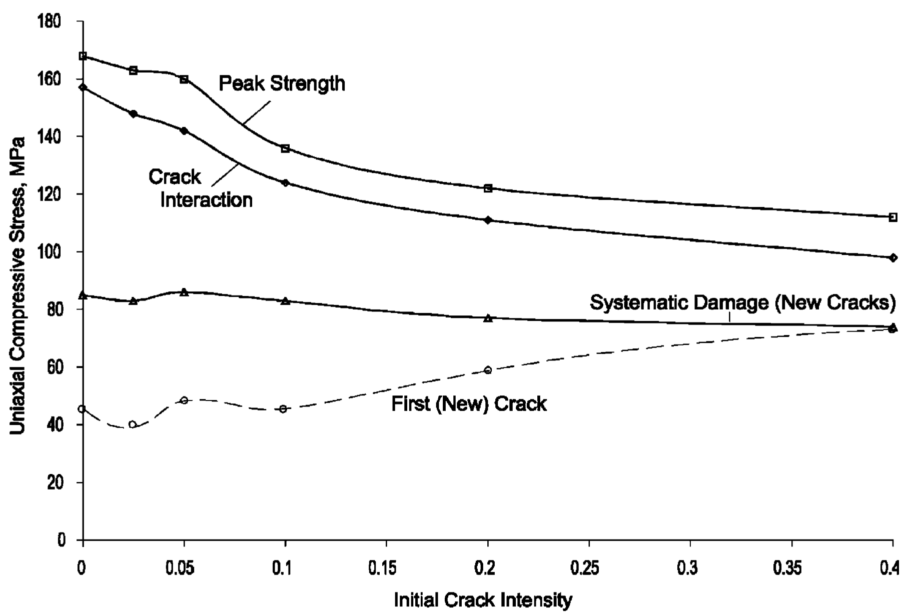

Fig. 25. Influence of pre-existing isotropic damage on key damage thresholds in 2D numerical simulations.

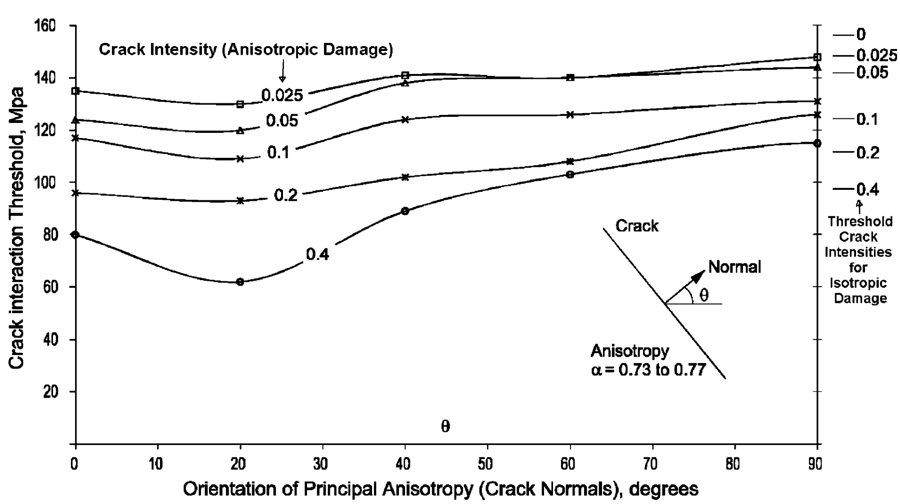

Fig. 26. Influence, on damage interaction threshold, of pre-existing, uniformly distributed crack damage at different initial intensities and preferred mean orientations.

on the crack interaction threshold is significant although not severe. The critical angle for strength reduction appears to be in the 20–25° range. This is consistent with the critical centre to centre angle for crack interaction proposed by Du and Aydim [55]. This means that existing cracks within this critical orientation range facilitate the interaction of new cracks, thereby reducing the new crack accumulation required for crack interaction and yield.

9. Effect of stress rotation on crack propagation

Stress rotation during tunnel development can create damage oriented at angles other than the final boundary-parallel crack directions normally associated with brittle rock damage. This effect was shown in the previous section to be significant, although not severe. Stress rotation can, however, also change the conditions of crack propagation.

Rotation of σ_1 and σ_3, for example, can result in crack extension. This mechanism, illustrated in the upper diagram in Fig. 27, works by utilizing the initial flaw and the new mode I wing cracks, generated via one stress orientation, as a composite driving flaw to extend additional wing cracks parallel to a new stress orientation. If the stresses are then returned to their original orientation, as is the case with the URL tunnel, the process repeats itself and the crack grows further. This interpretation is based on the fundamental fracture mechanics relationship between the length of a propagating crack and the length of the initial or causative flaw. In addition, the effect of rotation of σ_2 and σ_3 can be appreciated by considering a three-dimensional penny shaped crack as in the lower diagram in Fig. 27. The initial wing cracks are driven by the initial stress direction. In addition to confinement away from the driving flaw, pure geometrical constraints restrict the propagation of the 3D wing crack as it needs to propagate both around the perimeter of the old flaw as well as in the direction of the wing crack tip. A rotation of σ_2 and σ_3 creates favourable conditions for propagation around the perimeter as shown. This process is then further enhanced by a return to the initial conditions. Even small increases in wing crack length are significant as these increments may drive the crack beyond the constraining grain boundaries, leading to larger-scale propagation. Once a crack propagates beyond the grain boundaries, the constraining effect of the boundaries are significantly reduced or eliminated.

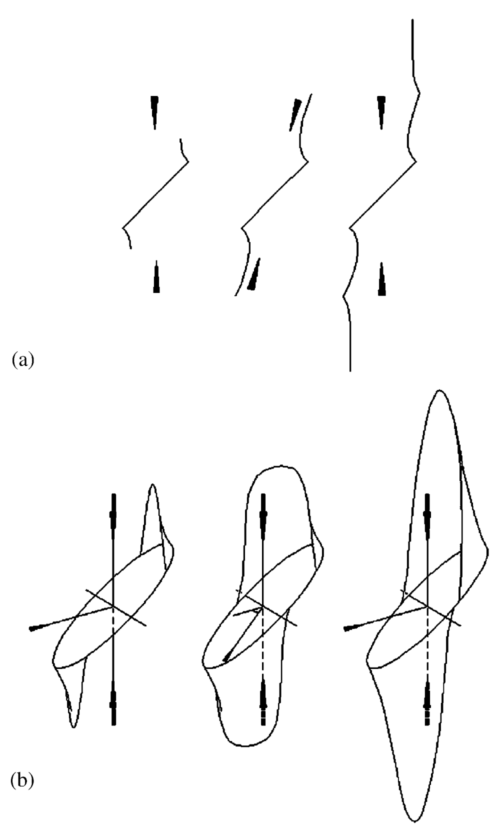

Fig. 27. Crack propagation through stress rotation: (a) rotation of sigma 1 and 3; (b) rotation of sigma 3 and 2.

Analysis of stress rotation effects on crack propagation can be carried out using available fracture mechanics software. It is also possible with a simple finite element program (e.g. PHASE[2] [56]). Here a staged stress path is modelled as shown in Fig. 28. This stress path is not unusual for tunnel development. Here a 25° rotation in the σ_3 direction is imposed during a progressive rise in deviatoric stress.

A simple crack tip is modelled using discontinuity elements within an isoparametric 6-noded triangular FEM mesh. A standard Mohr Coulomb criterion is employed with a tension cutoff. The loads are increased incrementally. At each stage the crack is extended according to the zone of new tensile rupture indicated by the FEM elements (no special crack tip element is employed and so the results must be considered subject to crack tip blunting and are as such conservative in their estimation of propagation). The applied stress orientation for one "sample" is rotated according to the stress path in Fig. 28 while the other is monotonic. The resulting crack growth is summarized in Fig. 29. The crack extension at the final stress state is approximately double in the rotated sample as compared to the monotonic sample. If the initial flaw is assumed to be controlled by the grain dimension, then this increase would certainly extend the crack beyond the grain boundaries and lead to crack interaction at a lower applied stress.

In addition to pure rotation, an increase in the intermediate principal stress during this process can also lead to enhanced spall damage. In axisymetric loading conditions where $\sigma_3 = \sigma_2$, critically oriented flaws

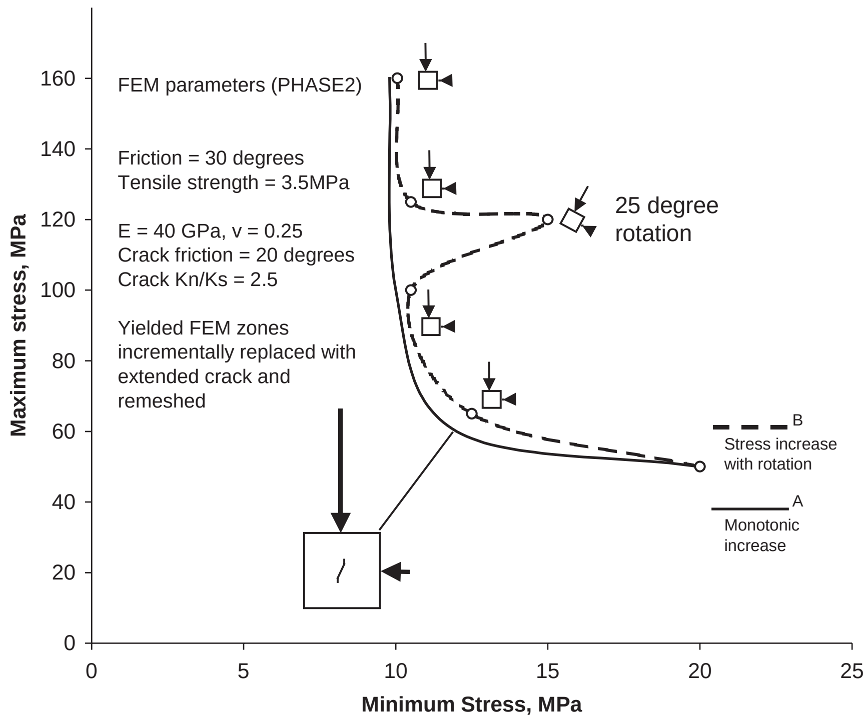

Fig. 28. Two stress paths simulated in Fig. 29. In this schematic example the intermediate stress is not considered. In situ conditions are indicated by the start of the curves at bottom right and the final state after the excavation has passed is represented by the upper terminations of the curves. The rotation of stresses is due to the passage of the tunnel face during excavation.

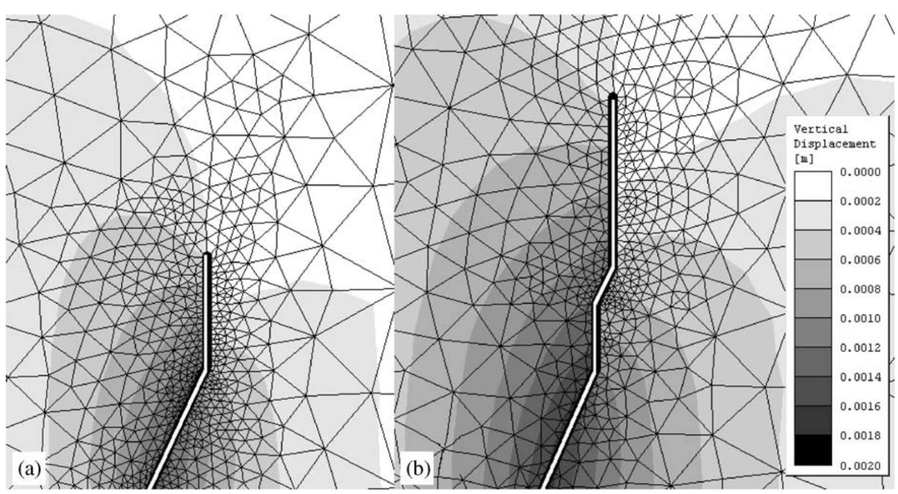

Fig. 29. Schematic finite element results for crack propagation. Field stresses are incrementally increased leading to tensile rupture at the crack tip. Ruptured elements are replaced incrementally with joint elements (tension-free) and analysis is then continued with increasing stress. Left image (a) is for monotonic stress path in Fig. 28. Right image (b) shows effect of stress rotation (stress path B in Fig. 28). Vertical displacement is plotted to highlight discontinuum deformation.

initiate cracks that extend parallel to the direction of σ_1. Only cracks that are within a small range of parallelism can interact to form macroscopic spall surfaces. Most of the cracks formed under these loading conditions, therefore have little contribution to the ultimate failure surface. Contrast this, as in Fig. 30, to the other extreme case of $\sigma_1 = \sigma_2$, and it is easy to see that cracks formed under these conditions all have similar orientation, normal to the direction of σ_3. These cracks will have a much greater potential to coalesce into macroscopic failure surfaces. If these cracks are parallel to the ultimate opening boundary, then the rock is preconditioned to spalling. If the cracks are at a slight angle to the ultimate tunnel boundary then kinematic freedom for failure is enhanced. This is significant as discussed in the following case example.

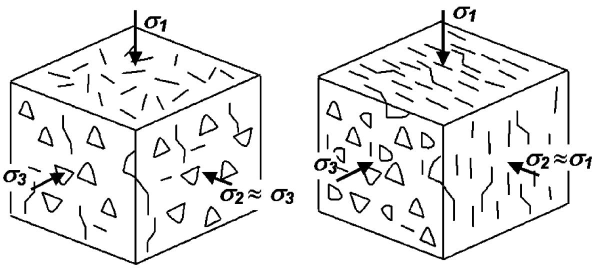

Fig. 30. Schematic illustration of crack initiation and propagation orientation under different conditions of intermediate principal stress: $\sigma_2 = \sigma_3$ (top) and $\sigma_2 = \sigma_1$ (bottom).

10. Stress rotation and damage—URL case study

At the Underground Research Laboratory in Pinawa, Manitoba (Canada), a circular test tunnel was driven in unjointed massive (plutonic) granite using a non-explosive "non-damaging" excavation procedure developed at the Underground Research Laboratory (URL) operated by Atomic Energy of Canada Ltd. (AECL). It has been analysed and well documented by numerous researchers [19,20,33,43] and by these authors.

Each round of the tunnel consisted of a dense and interconnecting circular pattern of perimeter drill holes to delineate a disk 1 m thick. This disk was then separated from the face using hand-held splitters. This process was intended to eliminate any excavation-induced damage. While the maximum boundary stress levels were significantly less than the strength of undamaged granite samples, crushing and spalling resulted in a large notch forming in the floor and roof of the test tunnel exposed after tunnel completion. The final depth of failure recorded in the zones of maximum notch formation are shown in Fig. 1 as the data from [19].

The rock exposed in the tunnel included both grey granites and granodiorites. The mineralogical composition and recorded grain sizes for the two units are shown in Fig. 31. The granites are more heterogeneous both in composition and in grain size. Of interest here is the fact that while the granite zones experienced tunnel overbreak equivalent to 40% of the tunnel radius, the granodiorites showed virtually no breakouts at all. This seems at odds with the observed ratio, σ_{ci}/σ_c of 0.45–0.5 for the granodiorites and a calculated boundary stress ratio, σ_{max}/σ_c of 0.7. According to Fig. 1, if the strength of the granodiorites had reduced to the lower bound represented by σ_{ci} (as was the case for the granites), the depth of failure in the granodiorites should have been on the order of 30% of the tunnel radius or approximately half a metre.

Part of the reason for this strength reduction difference is that the granodiorites are much finer grained and more homogenous than the granites at the URL. In addition, the lower bound strength (systematic

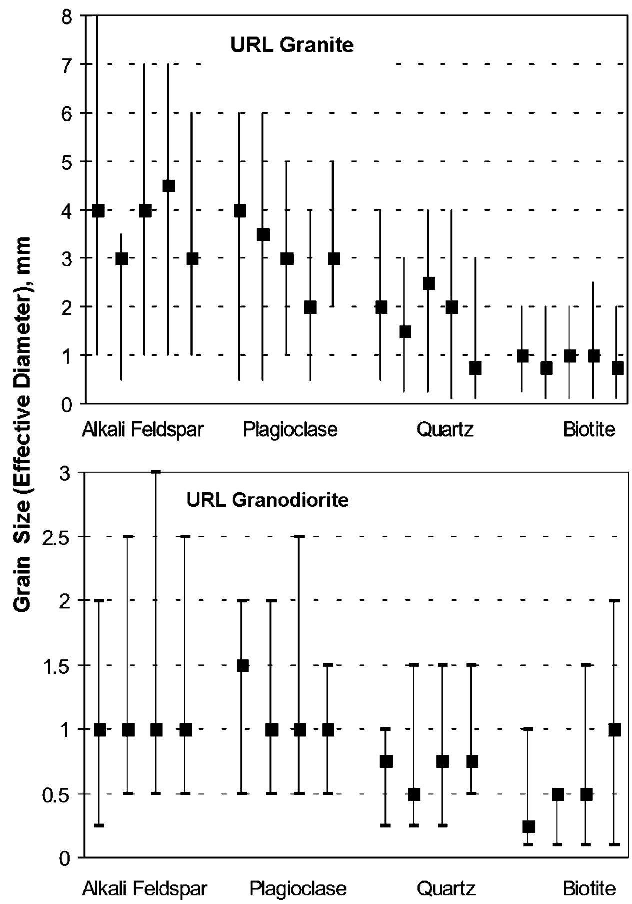

Fig. 31. Mineralogy and grain size distribution for grey granites and granodiorites at the Underground Research Laboratory (based on data from [57]).

crack initiation) for the granodiorites, as demonstrated in the examples of Figs. 14–17, is approximately 110 MPa while the granites have a lower bound strength of between 75 and 80 MPa.

The most significant reason for the difference in behaviour lies in a detailed examination of the stress path during the tunnel creation and specifically the rotation of stresses during this sequence. To this end, a three-dimensional elastic analysis (boundary element) was carried out on the test tunnel. Updated stresses from Martin [58] were used as input into the model. Recent studies have suggested that, contrary to original design intentions, the tunnel was aligned several degrees off the axis defined by the intermediate principal in situ stress [59]. This offset was not considered here and the tunnel is assumed to be parallel to σ_2. Detailed examinations of the stresses and the stress rotation, along a vertical plane (parallel to the tunnel axis) and around a circumferential surface 25 mm from the tunnel wall, are shown in Figs. 32 and 33, respectively. The orientation of σ_1, actually 11° off the vertical, has been rotated to the vertical for simplicity here.

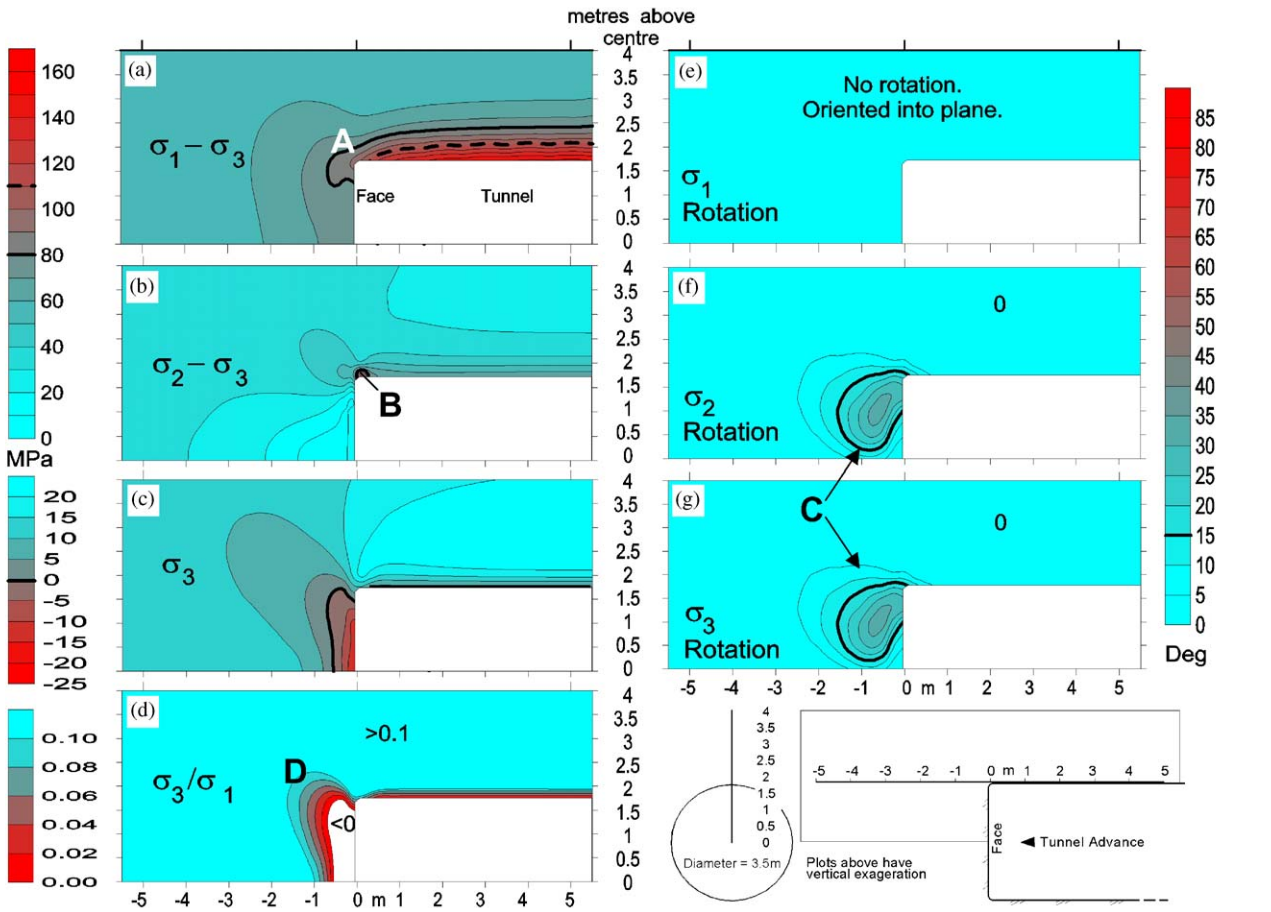

Fig. 32. (a)–(g) Plots of key stress variables on a vertical plane above the URL tunnel centreline, from –5 m to + 5 m from the advancing face. See text for explanation of labels A–D.

There are a number of points of interest in these plots. First there is a marked increase in deviatoric stress nearly 1 m in front of the advancing face (point A). The damage initiation thresholds for granite ($\sim$80 MPa) and granodiorite (110 MPa) are highlighted in bold and dashed contours, respectively, in the $\sigma1$–$\sigma3$ plots. Note that the damage initiation threshold for granodiorite is not exceeded until the tunnel has passed, while granite damage begins 1 m in front of the face. The σ_2–σ_3 plot indicates that the intermediate stress also exceeds the damage threshold for granite in a small zone immediately in front of the tunnel face (point B). Meanwhile, throughout this region in front of the face, the intermediate and minor principal stresses rotate through 25° and back again (points C). In addition, the minor/major stress ratio approaches zero and is even tensile in a small zone in front of the tunnel (point D). It is evident then that the zone in which the notch ultimately begins to form (the tunnel crown), undergoes stress levels above the damage initiation point for both major and intermediate principal stresses, well within the spalling limit for a heterogeneous granite, while significant stress rotation is taking place. The previous discussions have outlined the importance of all of these factors in the reduction of in situ strength. All of the foregoing occurs, however, below the damage initiation threshold for granodiorite. This is shown more clearly in Fig. 34. Here a stress path near the ultimate tunnel boundary is shown along with the stress rotation. While the granite undergoes the impact of numerous factors favourable for crack propagation, the granodiorite does not.

While damage initiates in the granodiorite, the propagation is not as enhanced as it is in the granite. As the tunnel passes, the net effect is that fracture development in the granite resembles the schematic simulation in Fig. 29b, while the granodiorite resembles Fig. 29a. In addition, the stress rotation in the granites leads to cracks oriented obliquely to the tunnel boundary.

New and propagating cracks forming just in front of the tunnel in the granite will also have an orientation non-parallel to the final tunnel boundary (i.e. they will be parallel to σ_3 in front of the face). After the tunnel advances past, they will have a dip towards the tunnel face. The orientation of these cracks is consistent with the observed structure within the "process zone" at the

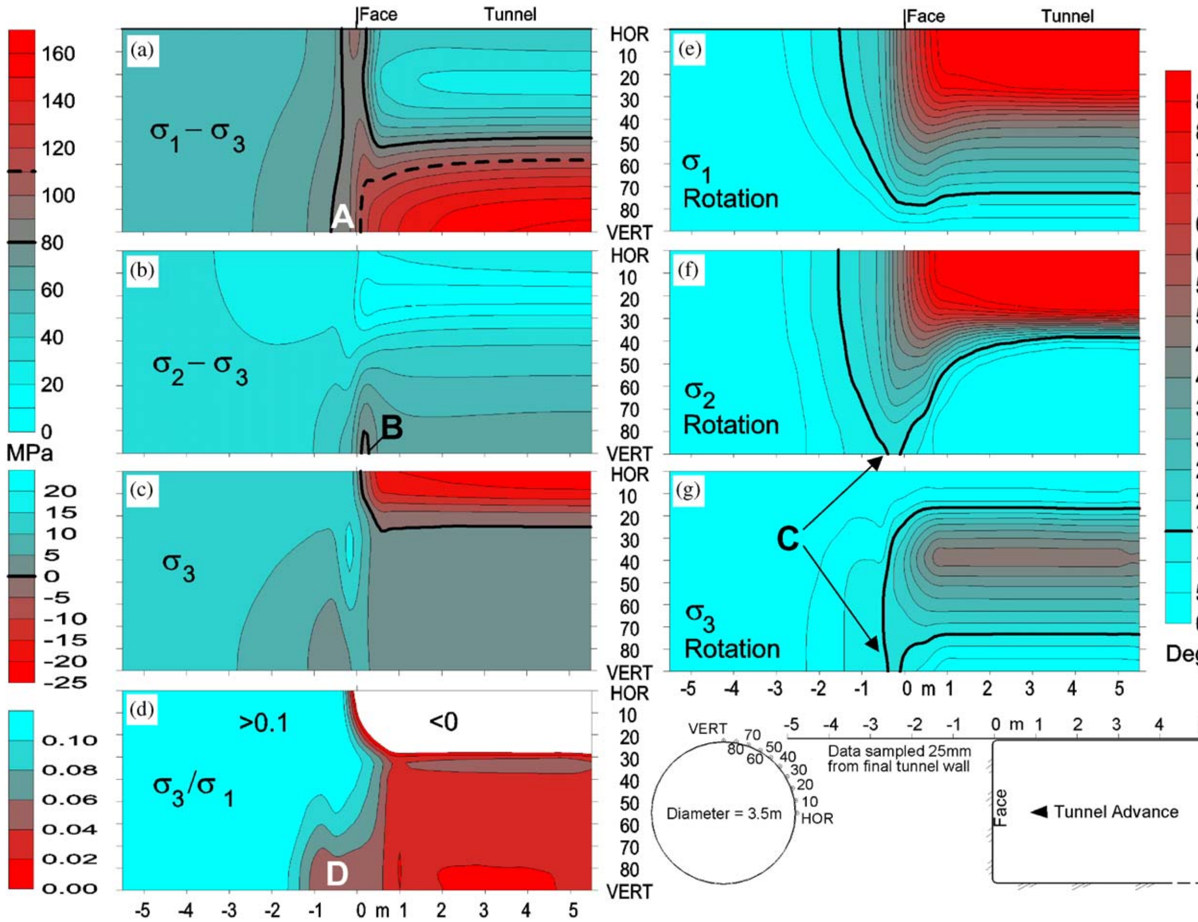

Fig. 33. (a)–(g) Plots of key stress variables on an unrolled surface 25 mm from the tunnel wall, from the crown to the springline. As indicated by the central axis, the top of each plot represents the stresses 25 mm into the rock from the tunnel springline while the bottom of each plot is just above the tunnel crown. Horizontal axis represents distance—5 m to +5 m from the advancing face. See text for explanation of labels A–D.

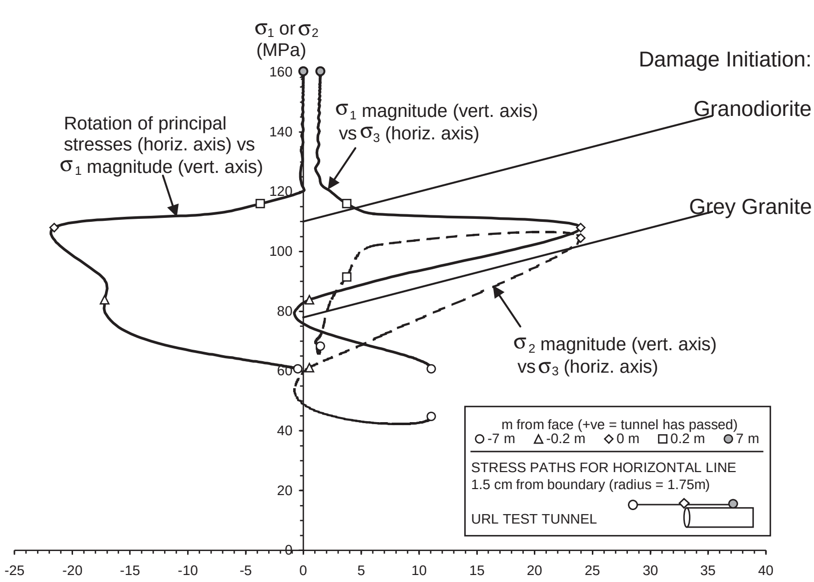

Fig. 34. Plot of stress paths (σ_1, σ_3 and σ_2, σ_3) and the maximum rotation angle for the principal stresss, for a point 1.5 cm from the tunnel crown as the tunnel advances past. The region of high intermediate stress and maximum stress rotation can be compared to the damage initiation thresholds for granite and granodiorite. For the granodiorite, the stress path is monotonic above this rock's threshold.

incipient notch. In other words, cracks in the granodiorite are likely to be purely boundary parallel and, without significant extension, lack of the kinematic freedom to "breakout" until higher stresses are reached—higher than the $0.7 \times \sigma_1$ ultimately experienced.

Finally, the elevated levels of the intermediate stress (above the initiation threshold for granite only) result in enhanced crack interaction and spall potential as illustrated in Fig. 30.

As a result of this study, which is by no means exhaustive (see [60] for more examples of tunnel-induced stress rotation in advance of tunnels and [61] for a discussion of stress rotation around excavation faces in mining), a provisional caveat has been added to the suggested lower bound strength calculations of Table 1. If UCS (in situ) calculated using the FSR technique ($\mathrm{FSR} \times \mathrm{UCS}_{\mathrm{lab}}$) is greater than 2/3 of the maximum boundary stress around the final tunnel ($2/3 \times \sigma_{\max}$) then use a default FSR of 0.7 or, if measured, use σ_{cd}/UCS.

This adjustment, which should be considered to be limited to situations of high in situ stress ratio, takes into account the combined effects (or lack of effects) of stress rotation, high intermediate stress and spall potential that occur above (or below) the crack initiation threshold. Rigorous examination of stress paths for other tunnel situations is warranted in order to more accurately apply this caveat. It is assumed here that if these effects occur below the damage initiation threshold, as for the granodiorite, then the reduction of strength from σ_{cd} to σ_{ci} is significantly ameliorated. The URL experience can be summarized as in Fig. 35.

It is critical to consider this effect when performing empirical calibrations or back analysis of failure observations. As with the granodiorite, the lack of failure may not be indicative of an elevated lower bound strength, but rather the absence of factors required to reduce strength to this minimum. If conditions change slightly (e.g., as in a 10% increase in stresses at URL) then the observed in situ strength of such rocks will drop significantly.

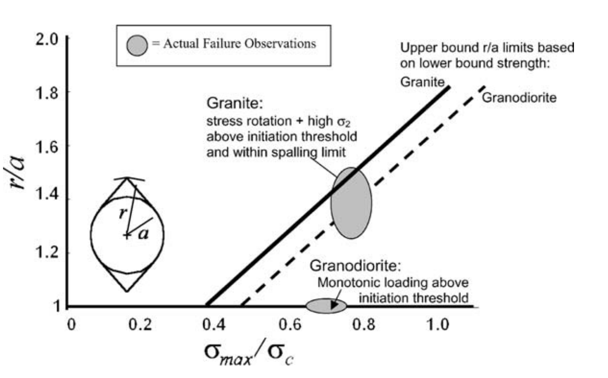

Fig. 35. Simplification of Fig. 1 illustrating the different behaviour of the granites and granodiorites at the URL test tunnel resulting from the fundamental differences in the stress paths in Fig. 34.

11. Conclusions

The importance of the two distinct mechanisms of crack initiation and crack interaction has been demonstrated. The first mechanism, initiation, defines a threshold in stress space that is a robust material property, relatively insensitive to numerous external factors and one that defines the lower bound for in situ strength of massive to moderately jointed rockmasses (sparce, discontinuous, rough, unfilled and clamped joints). Crack damage interaction gives rise to a strain-based threshold related, in laboratory tests, to a critical crack intensity required for the interaction and subsequent coalescence of damage into macroscopic failure surfaces. In confined conditions, these surfaces are actually shear zones composed of interacting extension cracks. In unconfined conditions, these surfaces manifest in the form of spalling. The difference here is the dominance, in low-confinement conditions, of the third mechanism, crack propagation. In laboratory conditions, crack damage accumulation progresses without significant crack propagation. In near-excavation conditions, however, cracks propagate upon initiation. Longer cracks lead to premature interaction and yield at a lower deviatoric stress level.

The crack initiation threshold can be determined from lateral strain measurements but more accurately from acoustic emission monitoring. This threshold represents a true lower bound for in situ strength. A preliminary classification system for estimation of this lower bound strength has been introduced based on mineralogy, grain size and heterogeneity.

The crack interaction and initial yield threshold can also be detected from acoustic emission studies and from axial stress–strain non-linearity. This threshold represents the true upper bound for in situ strength in both unconfined and confined conditions.

In the near excavation environment the degree to which strength degrades from the upper bound to the lower bound is controlled by small- and large-scale heterogeneity, the degree of pre-existing or excavation-induced damage and by stress rotation during tunnel construction. In particular, the effects of near-face stress rotation have been shown to yield profound impacts on the ultimate in situ yield stress and breakout potential of massive ground.

Understanding these mechanisms enables the engineer to better utilize semi-empirical relationships for depth of failure around tunnels in hard rock.

Acknowledgements

This work has been supported by the National Science and Engineering Research Council of Canada (NSERC) and by Atomic Energy of Canada Limited

(AECL). Special thanks Dr. Derek Martin for many years of input and discussion.

References

[1] International Society for Rock Mechanics: Commission on Standardization of Laboratory and Field Tests. Suggested methods for determining the uniaxial compressive strength and deformation of rock materials. Int J Rock Mech Min Sci Geomech Abstr 1979;15:319–68.

[2] Hoek E, Brown ET. Underground excavations in rock. London: Institute of Mining and Metallurgy; 1980. 358pp.

[3] Hoek E, Brown ET. Practical estimates of rockmass strength. Int J Rock Mech Min Sci 1998;34(8):1165–86.

[4] Hoek E, Carranza-Torres C, Corkum B. Hoek–Brown failure criterion—2002 edition. In: Hammah R, Bawden WF, Curran J, Telsnicki M, editors. Proceedings of NARMS 2002. Toronto: University of Toronto Press. 2002. p. 267–74.

[5] Marinos P, Hoek E. GSI—A geologically friendly tool for rockmass strength estimation. In: Proceedings of GeoEng2000 Conference (CDROM), Melbourne, Vol. 1. 2000. (Invited Lectures).

[6] Carranza-Torres C, Fairhurst C. The elasto-plastic response of underground excavations in rockmasses that satisfy the Hoek–Brown criterion. Int J Rock Mech Min Sci 1999;36(6):777–810.

[7] Nickson S, Sprott D, Bawden WF, Coulson A. A geomechanical study for a shaft wall rehabilitation program. In: Proceedings of 99th CIM Annual General Meeting, Vancouver: Canadian Institute of Mining; 1997. 20pp.

[8] Martin CD, Kaiser PK, McCreath DR. Hoek–Brown parameters for predicting the depth of brittle failure around tunnels. Can Geotech J 1999;36(1):136–51.

[9] Pelli F, Kaiser PK, Morgenstern NR. An interpretation of ground movements recorded during construction of the Donkin–Morien tunnel. Can Geotech J 1991;28(2):239–54.

[10] Brace WF, Paulding BW, Scholz C. Dilatancy in the fracture of crystalline rocks. J Geophys Res 1966;71(16):3939–53.

[11] Stacey TR, Page CH. Practical handbook for underground rock mechanics. Germany: TransTech; 1986. 145pp.

[12] Wagner H.Design,support of underground excavations in highly stressed rock. In: Proceedings of sixth ISRM Congress, Montreal. Vol. 3. Rotterdam: Balkema; 1987. p. 1443–57.

[13] Castro L, McCreath D, Oliver P. Rockmass damage initiation around the Sudbury Neutrino Observatory Cavern. In: Aubertin M, Hassani F, Mitri H, editors. Proceedings of Rock Mechanics—NARMS '96, vol. 2. Rotterdam: Balkema; 1996. p. 1589–95.

[14] Grimstad E, Bhasin R. Rock support in hard rock tunnels under high stress. In: Broch E, Myrvang, Stjern G, editors. Proceedings of the International Symposium Rock Support—Applied Solutions for Underground Structures NSCE, Lillehammer, Norway, 1997. p. 504–13.

[15] Diederichs MS. Instability of hard rockmasses: the role of tensile damage and relaxation. PhD thesis, University of Waterloo, 2000. 567pp.

[16] Kaiser PK, McCreath D, Tannant D. Canadian rockburst support handbook. Sudbury: Geomechanics Research Centre; 1995. 314pp.

[17] Kirsten HAD, Klokow J. Control of fracturing in mine rock passes. In: Proceedings of Fourth International Congress on ISRM, Montreux, Vol. 1. 1979. p. 203–10.

[18] Jiayou L, Lihui D, Chengjie Z, Zebin W. The brittle failure of rock around underground opengins. In: Maury, Fourmaintraux editors. Proceedings of the Conference on Rock Mechanics and Rock Physics at Great Depth, Pau France, Vol. 2. . Rotterdam: Balkema; 1991. p. 567–74.

[19] Martin CD. The strength of massive Lac du Bonnet granite around underground openings. PhD thesis, University of Manitoba, 1994. 278pp.

[20] Martin CD.Failureobservations,in situ stress domains at the Underground Research Laboratory. In: Maury, Fourmaintraux editors. Proceedings of the Conference on Rock Mechanics and Rock Physics at Great Depth, Pau France, Vol. 2. Rotterdam: Balkema; 1989. p. 719–26.

[21] Ortlepp WD, Gay NC. Performance of an experimental tunnel subjected to stresses ranging from 50 MPa to 230 MPa. In: Brown, Hudson, editors. Proceedings of the ISRM Symposium on Design and Performance of Underground Excavations. London: British Geotechnical Society; 1984. p. 337–46.

[22] Stacey TR, De Jongh CL. Stress fracturing around a deep level bored tunnel. J S Afr Inst Min Metall 1977;78:124–33.

[23] Illston JM, Dinwoodie JM, Smith AA. Concrete, timber and metals. New York: Van Nostrand Reinhold; 1979. 663pp.

[24] Griffith AA. 1924. Theory of rupture. In: First International Congress of Applied Mechanics, Delft, 1924. p. 55–63.

[25] Horii H, Nemat-Nasser S. Brittle failure in compression: splitting, faulting and brittle ductile transition. Trans Roy Soc London, Math Phys Sci 1986;319:337–74.

[26] Kemeny JM, Cook NGW. Crack models for the failure of rocks in compression. In: Desai, Krempl, Kiousis, Kundu editors. Constitutive laws for engineering materials: theory and applications, Vol. 2. Amsterdam: Elsevier; 1987. p. 879–87.

[27] Lajtai EZ, Carter BJ, Ayari ML. Criteria for brittle fracture in compression. Eng Fract Mechanics, 1990;37(1):25–49.

[28] Wong TF. Micromechanics of faulting in Westerly granite. Int J Rock Mech Min Sci Geomech Abstr 1982;19:49–64.

[29] Gramberg J. Anon-conventional view on rock mechanics, fracture mechanics. Rotterdam: Balkema; 1989. 250pp.

[30] Trollope DH. The mechanics of discontinua or clastic mechanics in rock problems. In: Stagg KG, Zienkiewicz OC, editors. Rock mechanics in engineering practice. London: Wiley; 1968. p. 275–320.

[31] Cook NGW. Müller lecture: why rock mechanics? In: Fujii J, editor. Proceedings of the International Congress on Rock Mechanics, Tokyo, vol. 3, 1995. p. 975–94.

[32] Tapponier P, Brace WF. Development of stress induced microcracks in Westerly granite. Int J Rock Mech Min Sci Geomech Abstracts. 1976;13:103–12.

[33] Cundall PA, Potyondi DO, Lee CA. Micromechanics-based models for fracture and breakout around the mine-by tunnel. In: Proceedings of the Canadian Nuclear Society International Conference on Deep Geological Disposal of Nuclear Waste, Winnipeg, 1996.

[34] Itasca. PFC-particle flow code. Modelling software. Version 1.0, Itasca Ltd., 1995.

[35] Diederichs MS. Keynote: stress induced accumulation and implications for hard rock engineering. In: Hammah R, Bawden WF, Curran J, Telsnicki M, editors. Proceedings of NARMS 2002. Toronto: University of Toronto Press; 2002. p. 3–14.

[36] Tang CA, Kaiser PK. Numerical simulation of cumulative damage and seismic energy release during brittle rock failure—part I: fundamentals. Int J Rock Mech Min Sci. 1998;35:113–22.

[37] Hommand FD, Hoxha JF, Shao M, Sibai G, Duveau. Endommagement de granites et de marnes: Essais mechaniques, identification des parameters d'un modele d'endommagement et simulation. Final report B RP O.ENG/O.LML 95.015, ENGS Laboratoire de Géomécanique, Nancy, 1995.

[38] Eberhardt E, Stead D, Stimpson B, Read RS. Identifying crack initiation and propagation thresholds in brittle rock. Can Geotech J 1998;35(2):222–33.

[39] Eberhardt ED. Brittle rock fracture, progressive damage in uniaxial compression. PhD thesis, University of Saskatchewan, 1998. 335pp.

[40] Pestman BJ, Van Munster JG. An acoustic emission study of damage development and stress-memory effects in sandstone. Int J Rock Mech Min Sci. 1996;33(6):585–93.

[41] Holcomb DJ. General theory of the Kaiser effect. Int J Rock Mech Min Sci. 1993;30:929–35.

[42] Villaescusa E, Seto M, Baird G. Stress measurements from oriented core. Int J Rock Mech Min Sci 2002;39:603–15.

[43] Martin CD, Read RS, Martino JB. Observation of brittle failure around a circular test tunnel. Int J Rock Mech Min Sci 1997;34(7):1065–73.

[44] Suorineni FT, Kaiser PK. Characteristic acoustic properties of sulphide ores and host rocks. In: Hammah R, Bawden WF, Curran J, Telsnicki M, editors. Proceedings of NARMS 2002. Toronto: University of Toronto Press; 2002. p. 403–10.

[45] Singh DP. A study of time-dependent properties, other physical properties of rocks. PhD thesis. University of Melbourne, 1970. 219pp.

[46] Fonseka GM, Murrell SAF, Barnes, P. Scanning electron microscope and acoustic emission studies of crack development in rocks. Int. J. Rock. Mech. Min. Sci. & Geomech. Abstr. 1985;22(5):273–89.

[47] Castro L. Analysis of stress-induced damage initiation around deep openings excavated in a moderately jointed brittle rockmass. PhD thesis, University of Toronto, 1996.

[48] Haied A, Kondo D, Henry JP. Strain localization in Fontainebleau sandstone. Mech Cohes-Fric Mater 2000;5:239–53.

[49] Bieniawski ZT. Mechanisms of brittle fracture of rock: Part I: Theory of the fracture process; Part II: experimental studies; Part III: fracture under tension and under long term loading. Int J Rock Mech Min Sci. 1967;4:395–430.

[50] Dyskin AV, Germanovich LN. Model of rockburst caused by cracks growing near free surface. In: Young RP, editor. Rockbursts and seismicity in mines. Rotterdam: Balkema; 1993. p. 169–74.

[51] Jardine AKS. Maintenance, replacement and reliability. London: Pitman; 1973. 200pp.

[52] Cho N, Martin CD, Christiansson R. Suppressing fracture growth around underground openings. In: Hammah R, Bawden WF, Curran J, Telsnicki M, editors. Proceedings of NARMS 2002. Toronto: University of Toronto Press; 2002. p. 1151–58.

[53] Hoek E. Brittle failure of rock. In: Stagg KG, Zienkiewicz OC, editors. Rock mechanics in engineering practice. London: Wiley; 1968. p. 99–124.

[54] Martin CD, Stimpson B. The effect of sample disturbance on laboratory properties of Lac du Bonnet granite. Can Geotech J 1994;31:692–702.

[55] Du Y, Aydin A. Interaction of multiple cracks and formation of echelon crack arrays. Int J Numer Meth Geomech 1991;15: 205–18.

[56] Rocscience. PHASE2 software: 2D finite element analysis of excavations. 2001.

[57] Kelly D, Peck DC, James RS. Petrography of granitic samples form the 420 m level of the Underground Research Laboratory, Pinawa, Manitoba. Contractor's report to AECL Research, Laurentian University, 1993.

[58] Martin CD. Seventeenth Canadian geotechnical colloquium: the effect of cohesion loss and stress path on brittle rock strength. Can Geotech J 1997;34(5):698–725.

[59] Read RS, Chandler NA, Dzik EJ. In situ strength criteria for tunnel design in highly stressed rockmasses. Int J Rock Mech Min Sci. 1998;35(3;):319–68.

[60] Eberhardt E. Numerical modeling of three-dimensional stress rotation ahead of an advancing tunnel face. Int J Rock Mech Min Sci 2001;38(4):499–518.

[61] Kaiser PK, Yazici S, Maloney S. Mining induced stress change and consequences of stress path on excavation stability—a case study. Int J Rock Mech Min Sci 2001;38(2):167–80.